university of groningen / faculty of science and engineering / kapteyn astronomical institute

Investigating the Dependence of the Baryonic j-M-f_{gas} Relationship on Different Star Formation Laws

ASTRONOMY BACHELOR RESEARCH PROJECT

July 4th, 2024

Andrea Costa, S4636708

Contact: a.costa@student.rug.nl, costa@astro.rug.nl

Supervisors: Prof.dr. F. Fraternali, Dr. G. Pezzulli

Abstract

Galaxy scaling relations connect essential properties of galaxies, providing insights into the mechanisms behind galaxy formation and evolution. A key example is the baryonic specific angular momentum-mass-gas fraction relation, whose fundamental origin is still an unresolved issue in astrophysics. This thesis investigates the dependence of the $j_{\rm bar} - {\rm M}_{\rm bar} - f_{\rm gas}$ relationship on different star formation laws. The study aims to test a semi-analytical galaxy evolution model using various star formation laws, including the classical Kennicutt-Schmidt law based on gas surface densities, a revised version of the Kennicutt-Schmidt law fitted with data that also includes low-density regions, and a law which also includes a dependence on the angular speed of the disk rotation. By implementing these laws, we aim to provide a more accurate prediction of star formation rates across different regions of galactic disks. The model assumes that gas accretes at progressively larger radii over time (i.e. inside-out growth), and introduces other assumptions, such as an exponential radial dependence of the rotation curve and the assumption of a constant rotational velocity over time, which were improvements over previous works.

Our model is able to reproduce the relation both qualitatively and quantitatively, supporting the concept of inside-out gas accretion. We show that the consideration of different star formation laws does not significantly affect the predicted $j_{\rm bar} - {\rm M}_{\rm bar} - f_{\rm gas}$ relation. Particularly, our results suggest that the more crucial ingredient of the model is the inside-out growth assumption. The (gas and stellar) surface density profiles using the new star formation laws are in better agreement with observations for the example galaxy NGC 2403. However, this analysis should be done with more galaxies before a definitive conclusion can be drawn. Future work should explore different parameter values for the accreting angular momentum, consider a star formation law based on volume densities, as well as revise other assumptions like the rotation curve functional form, with the aim of better reproducing the tight $j_{\rm bar} - {\rm M}_{\rm bar} - f_{\rm gas}$ relationship.

Table of Contents

1 Introduction

Galaxies come in various morphological types. In a classification based on the optical morphology, called the Hubble sequence, galaxies are subdivided into three categories: elliptical (early-type) galaxies, irregular and spiral (late-type) galaxies (Sparke & Gallagher, 2007). In this thesis, we focus specifically on spiral galaxies, also known as disk galaxies, which are characterized by their thin, rotating disk structure containing stars, gas, and dust. These galaxies exhibit spiral arms and have significant ongoing star formation.

Spiral galaxies, despite their diversity, share common features and tend to lie in tight scaling relations that link various physical properties (e.g. Tully & Fisher (1977), Fall (1983), McGaugh (2012), Marasco et al. (2021)). Studying these relationships is essential as it helps us understand the fundamental processes that drive galaxy formation and evolution. One such relationship links two key physical properties of galaxies: the angular momentum and the stellar or baryonic mass (see Romanowsky & Fall (2012), Kurapati et al. (2018), Mancera Piña et al. (2021a)). Recently, it has also been discovered that there is a dependency of that relationship with gas fraction (Mancera Piña et al., 2021b). Investigating the origin of this relationship can help uncover critical mechanisms that influence the evolution of galaxies over cosmic time.

1.1 Angular Momentum - Mass Relations

In this thesis, we will focus on the scaling relation that describes the dependency of specific angular momentum on the mass of the galaxy. The specific angular momentum is the angular momentum per unit mass, $j_i = \frac{J_i}{\mathrm{M}_i}$, where J is the angular momentum, M is the mass, and the subscript i indicates any of the three galaxy components: gas, stars, or baryonic content (the sum of gas and stars). Historically, this relation was first discovered for the stellar component by Fall (1983), and recently it has also been extended to the other components.

In recent years, interest has grown in the baryonic counterpart of the original Fall relation (see Obreschkow & Glazebrook (2014), Kurapati et al. (2018), Stevens et al. (2018), Zoldan et al. (2018)). In particular, the baryonic relation was shown to have a smaller intrinsic scatter compared to the stellar relation (Mancera Piña et al., 2021b). Moreover, it has been found that the baryonic angular momentum, at fixed mass, also has a relationship with the gas fraction, defined as the ratio of the gaseous mass to the baryonic mass, $f_{\rm gas} = \frac{\mathrm{M}_{\rm gas}}{\mathrm{M}_{\rm bar}}$ (Mancera Piña et al., 2021b). Figure 1 shows that there is a correlation, at fixed mass, between the baryonic specific angular momentum and the gas fraction, in the sense that higher gas fractions correspond to higher specific angular momenta. The best fitting relation found by Mancera Piña et al. (2021b) reads:

$$\log\left(\frac{j_{\rm bar}}{\mathrm{kpc\ km\ s^{-1}}}\right) = (0.73\pm0.02)\log\left(\frac{\mathrm{M}_{\rm bar}}{\mathrm{M}_\odot}\right) + (0.46\pm0.05)\log(f_{\rm gas}) - (4.25\pm0.19) \tag{1}$$

where $j_{\rm bar}$ is the specific angular momentum of the baryons. The $j_{\rm bar} - \mathrm{M}_{\rm bar} - f_{\rm gas}$ relation was found to have the lowest scatter compared to the stellar and gas relations, and was argued to be the most fundamental of the three by including all galaxy matter components. It has not yet been explained by theoretical models, however.

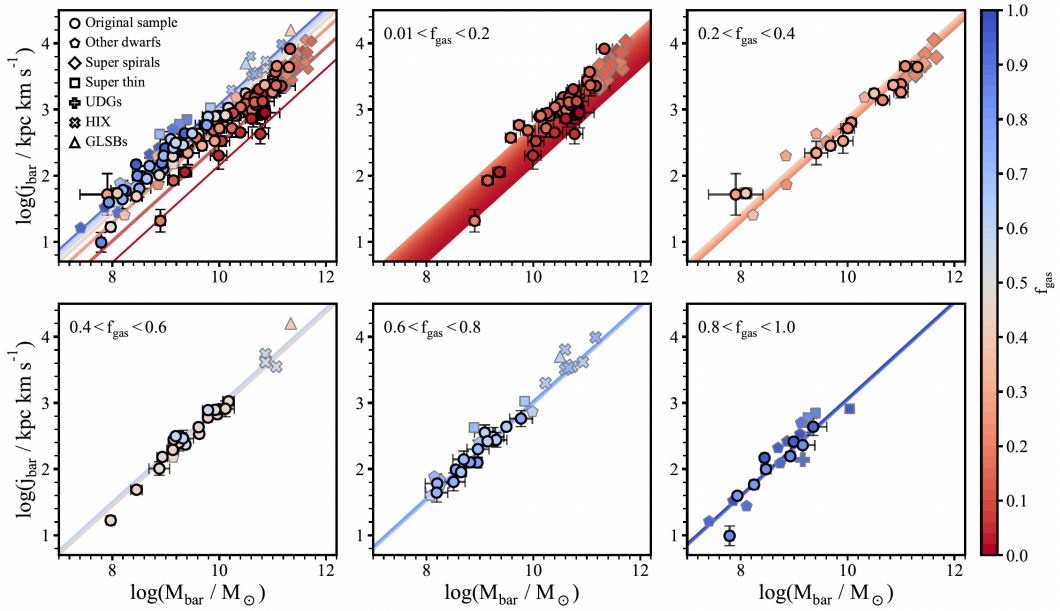

Figure 1: The relationship between the specific angular momentum ($j_{\rm bar}$) and baryonic mass ($M_{\rm bar}$) of galaxies, color-coded by gas fraction ($f_{\rm gas}$), as presented by Mancera Piña et al. (2021b). The top-left panel shows the relationship for all galaxies, with the constant gas fraction lines of best fit. The remaining panels show the relation for different ranges of $f_{\rm gas}$ (indicated on the top left of each panel). The shaded regions represent the regime delimited by the corresponding $f_{\rm gas}$ bin.

1.2 Gas Accretion

The main ingredient for star formation to take place is cold gas, which is present almost exclusively in disk galaxies. Despite this, the gas depletion time (i.e. the timescale over which the current gas reservoir would be consumed given the current rate of star formation) of disk galaxies is often rather short (Cimatti et al. (2019), hereafter CFN19). As a consequence, in order for galaxies to keep forming stars and not quench (cease their star formation processes), the gas reservoir in their disks reservoir needs to be constantly replenished. Gas replenishment occurs through a series of processes starting from the intergalactic medium (IGM), which contains vast amounts of diffuse gas between galaxies. This gas is expected to continuously accrete from the circum-galactic medium (CGM), a halo of gas surrounding individual galaxies. The CGM acts then as a reservoir that slowly feeds gas into the galaxy's disk. The infall of gas from the CGM into the galactic disk is driven by gravitational forces and radiative cooling, and this continuous inflow ensures that the star formation process can persist over cosmic timescales, preventing the galaxy from running out of the necessary raw material for forming new stars.

To date it is still not yet quite clear how gas accretion into galaxies takes place (e.g. Sancisi et al. (2008), Aumer & Binney (2009), Putman et al. (2012), Di Teodoro & Fraternali (2014)). In the case of the Milky Way, the observed star formation rate (SFR) is roughly 2 $M_\odot yr^{-1}$ (Murray & Rahman, 2010), and the star formation history suggests that it has been roughly constant throughout cosmic time (Aumer & Binney,

2009). Historically it was thought that High Velocity Clouds could have supplied enough gas to maintain star formation, however recent studies such as Putman et al. (2012) suggested that this could not contribute more than 0.08 $M_{\odot}yr^{-1}$. Another picture states that merger events could be responsible, however Di Teodoro & Fraternali (2014) posed an upper limit on the SFR from mergers to be about 0.28 $M_{\odot}yr^{-1}$. The latest analysis suggests that the source of the infalling gas is the inter-galactic medium (IGM), however the physical mechanisms that bring gas from the IGM to galaxies remain not well understood.

It has also been discovered that gas accretes onto the disks at progressively larger radii over cosmic time (see Larson (1976), Pilkington et al. (2012), Patel et al. (2013), Pezzulli et al. (2015)). This can be deduced indirectly from the properties of galaxies and it is a contributor to the phenomenon of inside-out growth of galaxy discs (Brook et al. (2012), Patel et al. (2013), González Delgado et al. (2015)). Being able to model galaxies that grow inside out is essential to have a realistic depiction of how galaxies form and evolve. The progressively increasing radius of gas accretion in galaxies is thought to be explained by the tidal torque theory, first proposed by Hoyle (1949), and later refined by Peebles (1969). This theory predicts that the large-scale structure of the universe influences the angular momentum evolution of galaxies. Under this theoretical framework, the gravitational interactions between neighboring galaxies result in tidal torques, which can cause the galaxies to gain angular momentum. Larson (1976) postulated that gas with low angular momentum cools and settles on shorter timescales than gas with high angular momentum. This implies that over time, as angular momentum increases due to the effects of the tidal torques, gas accretes at progressively larger radii (see also Mo et al. (2010), CFN19, and Frankel et al. (2019)).

1.3 Star Formation Laws

Star formation is one of the most studied physical processes in astrophysics. One aspect of great relevance for galaxy evolution models is the relationship between the rate of star formation and the amount of cold gas available at a given time. This relationship is called the star formation law (SFL), and has been thoroughly investigated. The first to propose of such a law was Schmidt (1959), who suggested a power-law relation between the star formation rate (SFR) and gas volume densities. After this seminal work, a massive amount of research has been carried out on the topic, and a particular turning point was reached when Kennicutt (1998) discovered a relationship between the SFR ($\Sigma_{\rm SFR}$) and gas ($\Sigma_{\rm gas}$) surface densities. The relationship, popularly known as the Kennicutt-Schmidt law (KS law), read $\Sigma_{\rm SFR} \propto \Sigma_{\rm gas}^{N}$, where the power $N \approx 1.4$ (Kennicutt, 1998), and can be seen in Figure 2.

Various versions of star formation laws have been proposed and investigated. Many authors have discovered that there appears to exist a certain regime in gas surface density ($\Sigma_{\rm gas} \lesssim 10\ M_{\odot}pc^{-2}$) below which the classical KS law breaks (see Figure 3), with the relation steepening and the scatter increasing (e.g. Boissier et al. (2003), Kennicutt et al. (2007), Bigiel et al. (2008), Bigiel et al. (2010), Bacchini et al. (2019), Bacchini et al. (2020)).

Some authors have suggested that the relationship only exists between the star formation rate and molecular gas, instead of molecular plus atomic gas (e.g. Bigiel et al. (2008), Leroy et al. (2008)). They argue that there is not clear relation with HI and this is the cause of the break that occurs at low surface densities, where HI dominates. Still, several proposals of new star formation laws have been made in order to find a law that does not show a break between high and low gas surface densities. One proposal suggested the inclusion of the angular velocity, Ω, in the relation, which read $\Sigma_{\rm SFR} \propto \Omega\Sigma_{\rm gas}^{n}$ (see Silk (1997), Elmegreen (1997), Kennicutt

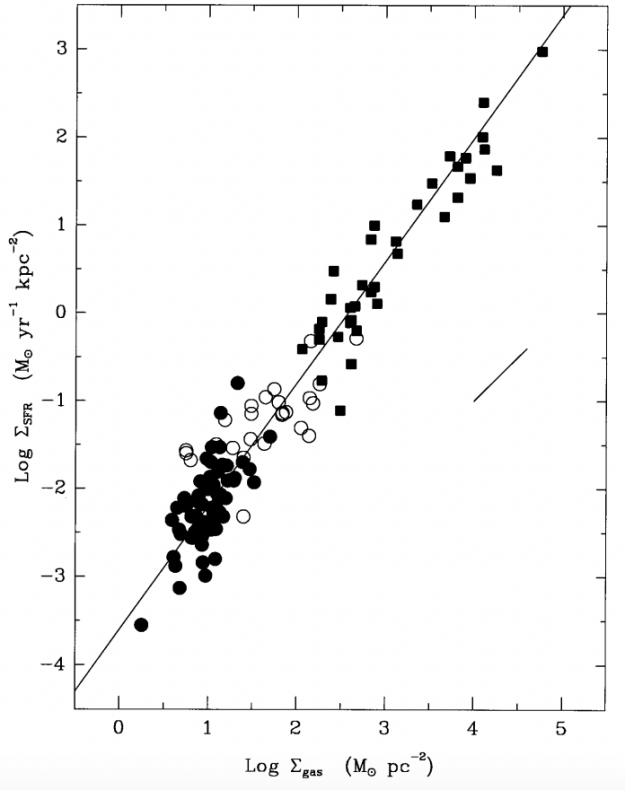

Figure 2: The original relation between the star formation rate surface density and the gas surface density found by Kennicutt (1998). The points correspond to individual galaxies, which also include starbursts, while the fit is shown in the graph as a solid black line.

(1998)). While they considered a linear relation ($n = 1$), Boissier et al. (2003) introduced an alternative and more general version of this law, which considered powers different from 1 ($\Sigma_{\rm SFR} \propto \Omega\Sigma_{\rm gas}^{n}$ for $n \neq 1$, hereafter known as the Boissier law).
Bacchini et al. (2020), instead, showed that if one models a star formation law using volume densities, the relationship (hereafter referred to as the volumetric star formation, VSF, law) has a very low scatter and appears not to show a break at the lower density regimes. VSF laws take into account the effects of disk flaring, which has been suggested by many as a cause behind the break in the SFR-gas surface densities relation (see Elmegreen (2018), Bacchini et al. (2019), Bacchini et al. (2020)). The relationship found was:

$$\rho_{\rm SFR} \propto \rho_{\rm gas}^{\alpha} \tag{2}$$

where $\alpha \simeq 2$ is the constant determining the slope, and $\rho_{\rm SFR}$ and $\rho_{\rm gas}$ are the star formation rate and gas volume densities, respectively. The adoption of volumetric densities, instead of surface densities, is also in better alignment with the early predictions made by Schmidt (1959) regarding the nature of star formation laws.

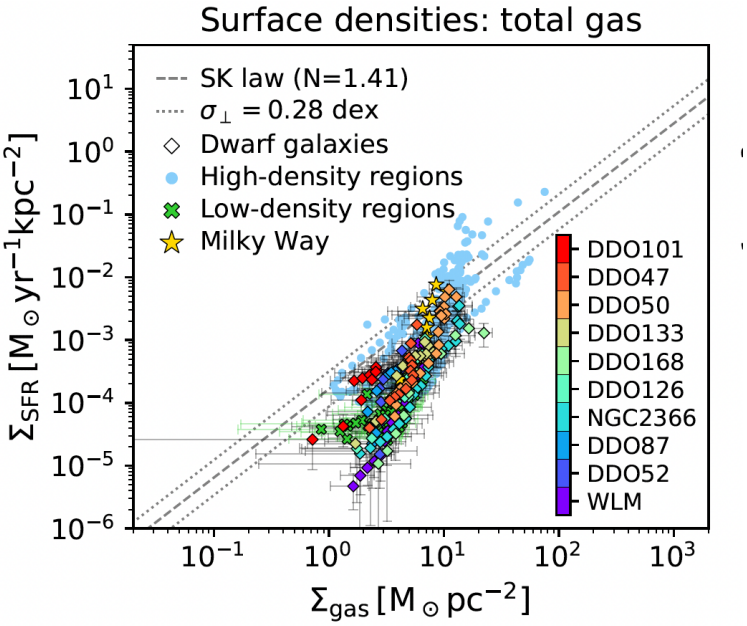

Figure 3: Star formation rate surface density versus gas surface density including low density regions and dwarf galaxies. There is a clear break in the KS relation. Plot taken from Bacchini et al. (2020).

It is crucial to highlight that the star formation law proposed by Bacchini et al. (2020) shares a similarity with the Boissier law. While the volumetric star formation law does not explicitly include the angular velocity, it accounts for the height of disks, which is related to the angular velocity. The angular velocity, Ω, relates to the disk's vertical component of the gravitational field, which balances against the gravitational pull of the disk and the dark matter halo. This balance determines the disk's vertical structure and thickness. Regions of the disk with higher angular velocity typically have greater rotational support, leading to thinner disks, whereas regions with lower angular velocity have less rotational support, resulting in thicker disks. The volumetric star formation law has been show to works well in both the inner and outer regions of massive and less massive galaxies. However, unlike the classical KS law, which includes data from extreme environments such as starbursts (as considered by Kennicutt (1998)), the volumetric star formation law has not yet been tested in these conditions. It is clear that, despite the great progress in recent years, a fundamental law of star formation has not been fully reached, and is still an open question.

1.4 Models of the $j_{\rm bar}$-M$_{\rm bar}$-$f_{\rm gas}$ Relation

A theoretical explanation of the $j_{\rm bar}$-M$_{\rm bar}$-$f_{\rm gas}$ relation requires to treat fundamental concepts of galaxy evolution, such as gas accretion and star formation. An early model developed by Camilleri (2022) attempted to predict this behavior, but did not have a good quantitative agreement with the data. In particular, that model assumed that galaxies do not evolve inside-out, and had gas accreting at constant radii. Furthermore, it used the classical Kennicutt-Schmidt law (Kennicutt, 1998) as the main star formation law, and it assumed a rotational velocity that is flat radially (i.e. constant with radius) and that evolves following the baryonic

Tully-Fisher relation (BTFR), which was assumed to not evolve in time.

The results of the model showed a qualitative prediction of the correlation found between $j_{\rm bar}$ and $f_{\rm gas}$ at fixed mass. However, it underpredicted the values of the gas fraction when using the standard KS law (0.13 to 0.43 with an accretion timescale of 25 Gyr). They also considered a revised version of the KS law by Gatto et al. (2013), which included dwarf galaxies, and in this case the gas fractions were found to be very high for all galaxies, again not reproducing quantitatively the data of Mancera Piña et al. (2021b). The results using the two star formation laws mentioned can be seen in Figure 4.

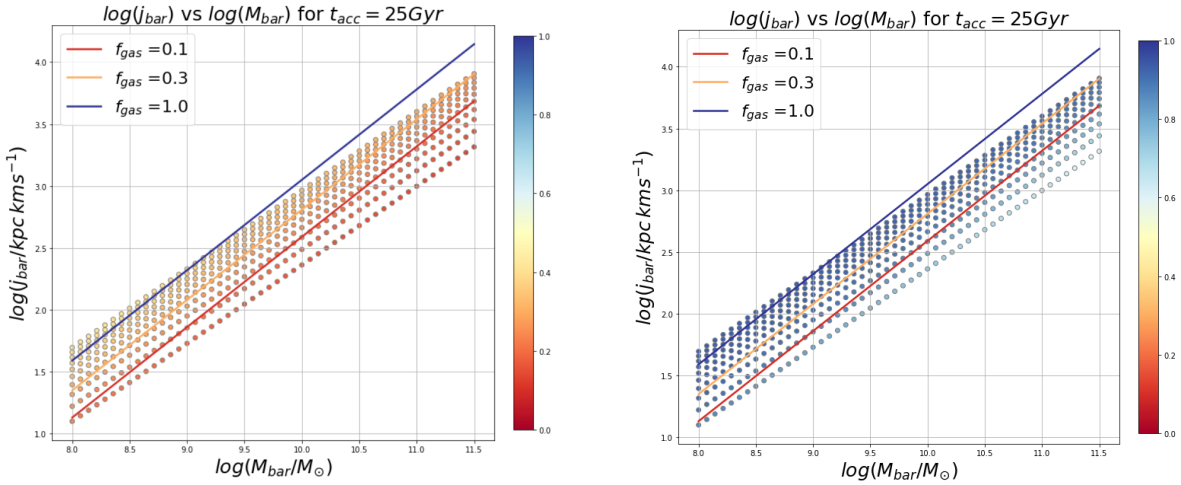

(a) Results using standard KS law

(b) Results using revised KS law by Gatto et al. (2013)

Figure 4: Results of the work carried out by Camilleri (2022) using the standard KS law (left) and the revised KS law from Gatto et al. (2013) (right). The points correspond to the model results, while the solid lines correspond to the empirical relation found by Mancera Piña et al. (2021b) for different constant $f_{\rm gas}$ values.

An improved version of this model was more recently developed, which also used the classical KS law, but employed an inside-out growth framework (Costa, 2023). This model was able to better predict the observational data by Mancera Piña et al. (2021b), in particular the gas fraction (see Figure 5). Nonetheless, the model had limitations in the predictions of spatially resolved internal properties of the galaxies, such as the gas and stellar surface densities, when compared to observations. In addition, it assumed the standard KS law, which as explained before is limited to high density regions. This indicates that the next step would be to investigate the model using different, and possibly more robust, star formation laws.

1.5 Scope of the study

This research thesis aims to explore the dependence of the baryonic j-M-$f_{\rm gas}$ relation on different star formation laws by building a model that describes the structural evolution of galactic disks. To achieve this, we will use three star formation laws: the classical Kennicutt-Schmidt law, and two other star formation laws — a revised version of the Kennicutt-Schmidt law, and the Boissier law —derived by fitting data from Bacchini

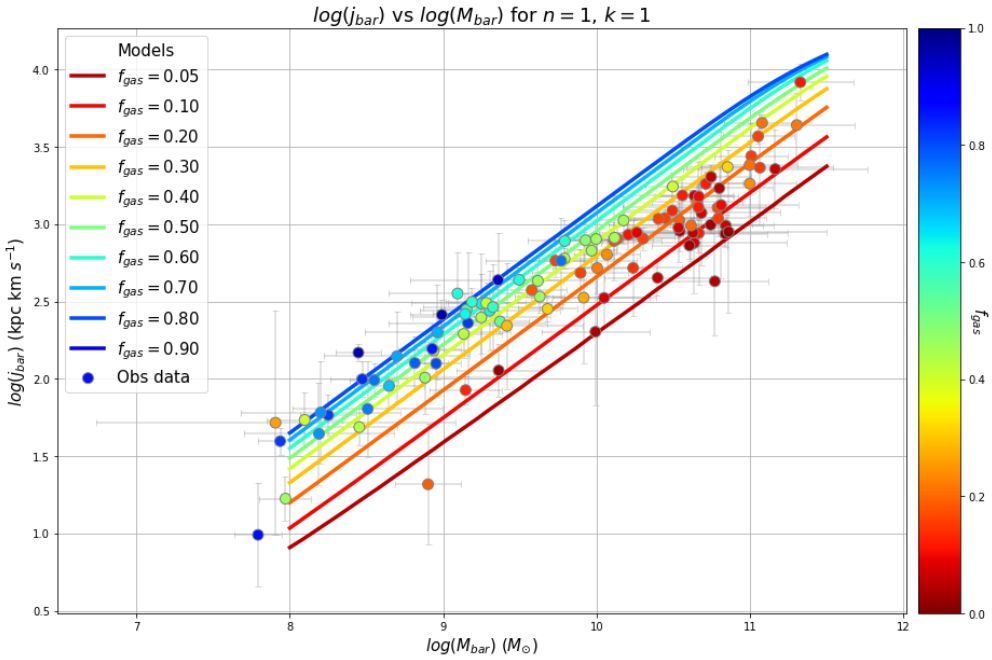

Figure 5: Final results from a preliminary work which included the inside-out growth framework (Costa, 2023). The colored circles are galaxy measurements by Mancera Piña et al. (2021b), whereas the solid lines correspond to the predicted constant $f_{\rm gas}$ values.

et al. (2020) (see Section 2.2.3). This data includes observations of the outer regions of galaxy disks, as well as the inner regions, and therefore can more accurately represent the full extent of gas densities in galaxies. The fits will then be implemented into the model based on the work by Costa (2023). The model will then be tested by investigating how it responds to changes in the parameters that define the gas accretion rate. Finally, a direct comparison between the model predictions and the observational data by Mancera Piña et al. (2021b) will be carried out.

To construct a SFL that includes an angular velocity term (Ω), further modifications in the model need to be made. In particular, the rotation curve cannot be flat radially (i.e. constant with radius), otherwise $\Omega \to \infty$ at low radii. To achieve this, an exponential rotation curve will be used instead, which avoids the division by zero, but has two more degrees of freedom. This requires two parameters to be fitted, for which data from the SPARC spiral galaxy catalogue will be used (Lelli et al., 2016).

Another improvement to the Costa (2023) model involves treating the rotational velocity as independent of time, meaning it will remain constant throughout the galaxy's evolution. This will be accomplished by determining the rotational velocity using the present-day value predicted by the Baryonic Tully-Fisher Relation (BTFR) (McGaugh, 2012). This value will then be kept constant throughout the evolution (giving a constant rotational velocity in time). This modification addresses an inconsistency in the previous model, where the rotational velocity increased over time even for gas that accreted at a certain radius early in the

galaxy's evolution. Such an increase would result in additional angular momentum that cannot be physically explained, leading to the inconsistency.

Chapter 2 will introduce the methodology needed to construct the model, along with an explanation of all the necessary assumptions and steps. There we also present the results of the fits done for the star formation laws and rotation curves. The results of the galaxy evolution models will then be obtained and presented in Chapter 3, illustrating in particular the dependence on the SFLs, and comparing the model predictions with the Mancera Piña et al. (2021b) observational data. After this, a discussion of the results will be made in Section 4, also outlining steps for further research. Lastly, in Section 5 a summary will conclude the thesis.

2 Research Methodology

In this work, the aim is to investigate the $j_{\rm bar} - {\rm M}_{\rm bar} - f_{\rm gas}$ relation and further improve previous models, as discussed in Section 1.1. The type of models we are developing are models that describe the evolution in time and space of disk distributions of gas and stars. A key ingredient of these models is the star formation law, a fundamental relation between the star formation rate of a galaxy and the cold gas content and, in some cases, other properties. Until now, many models have made use of the Kennicutt-Schmidt law (Kennicutt, 1998), which correlates the star formation rate surface density with the gas surface density (e.g. Pezzulli & Fraternali (2016), Fraternali & Tomassetti (2012), Camilleri (2022)), and only recently were volume densities also considered (Bacchini et al., 2020). One aim of this work is to evaluate the impact of different star formation laws on the predictions of the models, with emphasis on the specific angular momentum and gas fraction, as a function of baryonic mass. Furthermore, in order to model the rotation velocity of galaxies, the Baryonic Tully-Fisher relations (BTFR) (McGaugh, 2012) has been often used. The BTFR is an empirical relation that correlates the mass or intrinsic luminosity of a disk galaxy, with the asymptotically flat rotation velocity. In the previous model this relation was assumed to not evolve in time, implying that the rotation velocity at fixed mass increases with time (Costa, 2023). This causes inconsistencies in disk evolution models: at fixed radii the rotation velocity increases and produces an additional contribution to the angular momentum that cannot be physically explained. Therefore, another aim of this work is to apply another assumption, where the rotation velocity is kept constant in time throughout the evolution.

2.1 Structural evolution of disk galaxies

A model that describes the structural evolution of disk galaxies aims to simulate various processes taking place within the galaxy. For this purpose, the galactic disk is often divided into concentric and coplanar annuli of radius R. In this thesis, we will assume that the every annulus evolves independently, which means that we neglect flows of gas and migration of stars across the disk in the radial direction. This assumption, called the approximation of independent annuli, is an important simplification that is often used (e.g. Fraternali & Tomassetti (2012)). While not being true in reality, Fraternali & Tomassetti (2012) showed that this does not impact the results of disk evolution models significantly, while greatly simplifying the calculations.

Disk evolution models have several key ingredients: (cold) gas accretion, star formation, and gas outflows. These processes govern the evolution of star and gas surface densities ($\Sigma_{\rm gas}$ and $\Sigma_\star$, respectively) over time, which are described by the following equations (CFN19):

$$\frac{{\rm d}\Sigma_{\rm gas}}{{\rm d}t} = \dot{\Sigma}_{\rm eff} - \dot{\Sigma}_{\rm out} - \Sigma_{\rm rSFR} \tag{3}$$

$$\frac{{\rm d}\Sigma_\star}{{\rm d}t} = \Sigma_{\rm rSFR} \tag{4}$$

where each term depends on radius R and time t. Here, $\dot{\Sigma}_{\rm eff}$ is the effective gas accretion rate surface density, which can be further described as the actual gas accretion rate ($\dot{\Sigma}_{\rm acc}$), subtracting the gas flow to the adjacent disk annuli (CFN19). Furthermore, $\dot{\Sigma}_{\rm out}$ is the gas outflow rate surface density, $\Sigma_{\rm gas}$ is the sum of atomic and molecular gas surface densities ($\Sigma_{\rm gas} = \Sigma_{\rm HI} + \Sigma_{\rm H2}$), and $\Sigma_{\rm rSFR}$ is the reduced star formation rate surface

density (see section 2.1.1). For our purposes, it is assumed that there are no gas flows radially within the galaxy and that there is no loss of gas due to outflows. As such, $\dot{\Sigma}_{\rm eff} = \dot{\Sigma}_{\rm acc}$, and $\dot{\Sigma}_{\rm out} = 0$. For massive galaxies, where outflow speeds are significantly lower than escape speeds, outflows are often ignored, and the assumption holds well (CFN19).

2.1.1 Reduced Star Formation Rate

In order to simplify equation 4 and have an analytical solution, the Instantaneous Recycling approximation (IRA) was assumed. This approximation implies that a fraction of gas used to form stars is returned to the interstellar medium (ISM) on very short temporal scales (Prantzos, 2008). Under IRA, stars that are less massive than $1M_{\odot}$ live indefinitely, while stars more massive than this end their life cycle instantaneously. Therefore, the IRA becomes a good approximation when long temporal scales are considered, since the fraction of gas $\Re$ returned by a co-eval stellar population tends to a constant value for times ¿ a few Gyrs (Fraternali & Tomassetti, 2012). From this, we can define the reduced SFR surface density ($\Sigma_{\rm rSFR}$) as:

$$\Sigma_{\rm rSFR} = (1 - \Re)\Sigma_{\rm SFR} \tag{5}$$

where $\Sigma_{\rm SFR}$ is the star-forming rate surface density. The value of the return factor $\Re$ was chosen to be 0.30, following the work by Fraternali & Tomassetti (2012). This value can be derived if a Salpeter initial mass function (IMF) is assumed. The IMF describes the initial distribution of the masses of the stellar population of a galaxy and therefore impacts the value of the return factor. However, Fraternali & Tomassetti (2012) found that this factor does not change significantly with the use of other IMFs that are often used, such as the Chabrier (Chabrier, 2003) and Kroupa (Kroupa et al., 1993) IMF (0.32 and 0.31, respectively, or 0.46 for Chabrier if a high-mass flatter IMF is assumed).

2.2 Star Formation Laws

Star formation laws describe the relationship between the rate at which new stars are formed and the properties of the cold gas used to fuel the star formation process. These empirical laws are crucial for understanding how galaxies evolve over time.

2.2.1 Kennicutt-Schmidt Law

The Kennicutt-Schmidt law (KS law) is one of the first and most widely used star formation laws. It was initially discovered by Schmidt (1959) and later refined by Kennicutt (1998). The KS law reads:

$$\Sigma_{\rm SFR} = A\Sigma_{\rm gas}^{N} \tag{6}$$

where $\Sigma_{\rm gas}$ is the gas surface density, and A and N are constants. The values of the parameters A and N were determined by Kennicutt (1998) to be 0.1625 and 1.4, respectively, if $\Sigma_{\rm gas}$ is measured in $M_{\odot}pc^{-2}$ and $\Sigma_{\rm SFR}$ in $M_{\odot}pc^{-2}Gyr^{-1}$ (see also Pezzulli & Fraternali (2016) and Fraternali & Tomassetti (2012)).

A significant limitation of the KS law, as highlighted by Bacchini et al. (2020) and explained in the introduction (Section 1.3), is that the relation steepens considerably at lower surface densities, and the scatter increases. This behavior is particularly problematic in the outer regions of galactic disks, which are often HI-dominated,

lower-density, environments (e.g. Bacchini et al. (2019), Boissier et al. (2003), Bigiel et al. (2008), Kennicutt et al. (2007)). To address these issues and improve the accuracy of our models, we propose two key modifications: 1) We consider a different fit for the KS law that better represents the conditions in the outer disks. These regions are crucial for our models, which extend up to 100 kpc in radius, and an improved fit is expected to improve the results. 2) We explore an alternative formulation of the star formation law, specifically the Boissier law (Boissier et al., 2003), which includes a dynamical timescale factor (see Section 2.2.2). By implementing these modifications, we aim to provide a more accurate representation of star formation in the outer regions of galaxies, as well as to improve the overall predictive power of the model.

2.2.2 Boissier Law

The Boissier Law modified the original KS law by including a dynamical timescale factor:

$$\Sigma_{\rm SFR} = \alpha \Sigma_{\rm gas}^{n} \Omega(R) \tag{7}$$

where $\Omega(R) = 1/\tau_{\rm dyn} = \frac{V(R)}{R}$ is the angular velocity, the inverse of the dynamical timescale (see Boissier et al. (2003), Silk (1997), Elmegreen (1997)), and α and n are constants. This relation was shown by Boissier et al. (2003) to better fit galaxies at lower surface densities because of the inclusion of the dynamical timescale factor. This factor accounts for the time it takes for gas to respond to the gravitational potential of the galaxy, which improves the physical relevance. Boissier et al. (2003) reports a value of n of 1.48, however this was determined with a relatively low sample size of galaxies, as well as no value of α being reported. Therefore, similarly to the KS relation, we made our own fit to determine these parameters.

2.2.3 Star Formation Law Fits

The SFL fits were made with a sample of 22 local galaxies (including spiral and dwarf) prepared by Bacchini et al. (2020). This sample included data on the gas and star formation rate surface densities, as well as the asymptotic rotation curve velocities. For the dwarf galaxies, the gas surface densities and rotation velocities were obtained by Iorio et al. (2017) by analyzing the HI kinematics of galaxies from the LITTLE THINGS sample (Hunter et al., 2012), using the 3D-Barolo software (Di Teodoro & Fraternali, 2015). The SFR surface densities were instead determined by Bacchini et al. (2020), using azimuthally averaged surface photometry (with far-ultraviolet images, FUV), obtained from Zhang et al. (2012), and calibrating for SFR, using the SFR-FUV relation by McQuinn et al. (2015). For the spiral galaxies, on the other hand, the data were taken from the THINGS sample. Specifically, the HI and SFR surface densities were derived by Leroy et al. (2008) with a combination of FUV and 24 μm images. Instead, the H2 surface densities were derived by Frank et al. (2016), which used the same data as Leroy et al. (2008) but converted the HI into H2 with a CO conversion factor taken from Sandstrom et al. (2013). Lastly, the rotation velocities were derived by Bacchini (2020) (see also Bacchini et al. (2019)).

Figure 6 shows the data from Bacchini et al. (2020), overlaid with the fits of the SFLs. The gas surface densities were also corrected for helium, with a factor of 1.33 ($\Sigma_{\rm gas} = 1.33\Sigma_{\rm HI}$) (Mancera Piña et al., 2021b). Figure 6a shows the fit for the KS law, plotting the SFR surface density against the gas surface density, while Figure 6b shows the SFR surface density divided by the angular velocity, Ω, plotted as a function of the gas surface density.

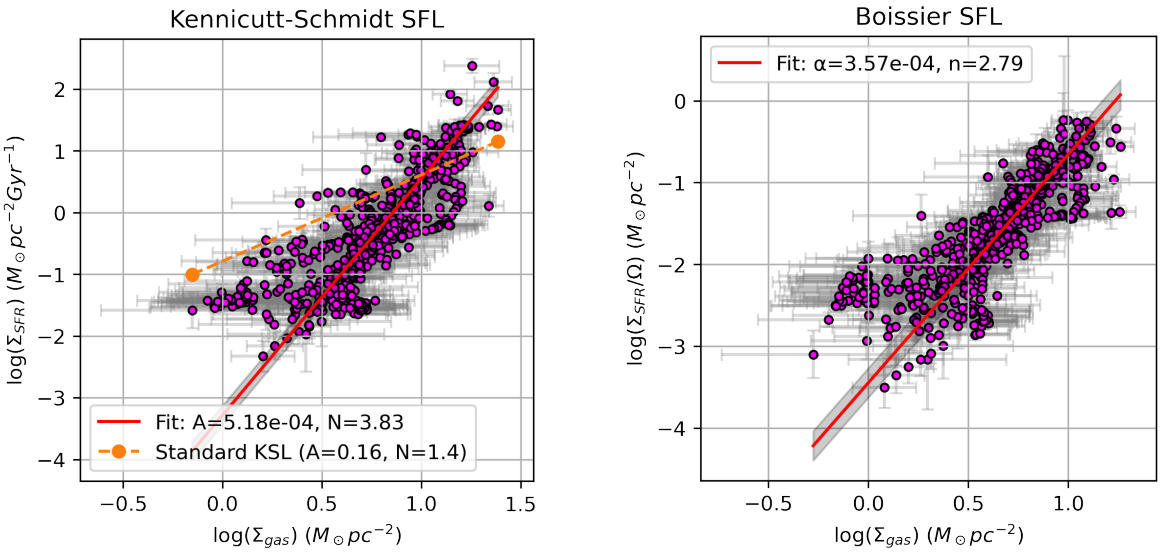

(a) Kennicutt-Schmidt SFL

(b) Boissier SFL

Figure 6: Fit of various star formation laws. The left plot (a) shows the star formation rate surface density versus gas surface density. The right plot (b) shows the star formation rate surface density divided by the angular frequency (in units of Gyr^{-1}) versus gas surface density. Both plots contain the fit (red line, with uncertainty in the gray area) made with the software BayesLineFit by Lelli et al. (2019). The left plot also contains the standard KS law such that a direct comparison can be seen. See Appendix A for the Bayesian fit parameter posterior distributions.

From Figure 6a, it is apparent that the relation breaks at lower densities, and the standard KS law (orange dashed line) over-predicts the star formation rate, causing too many stars to be formed in the outer regions of the disks. Our fit more powerfully predicts the star formation rate in these regions, which are common in our model. Furthermore, the Boissier law fit in Figure 6b shows a strong correlation with the data.

2.3 Gas Accretion History

One of the fundamental assumptions of our model is that the rate of accretion of gas is taken to exponentially decay in time, as follows:

$$\dot{\mathrm{M}}_{\rm acc}(t) = Ce^{-\omega_{\rm acc} t} \tag{8}$$

where $\dot{\mathrm{M}}_{\rm acc}$ is the gas accretion rate mass, $\omega_{\rm acc} = 1/t_{\rm acc}$ is an accretion frequency (the inverse of the accretion timescale), and C is a normalization constant that can be calculated by imposing a value of the total accreted baryonic mass at a given time. Positive values of $\omega_{\rm acc}$ mean that the gas accretion rate decreases exponentially over time, meaning most of the gas is accreted early in the galaxy's evolution. Conversely, negative $\omega_{\rm acc}$ values imply that the gas accretion rate increases exponentially over time, resulting in more gas being accreted later in the galaxy's evolution. To explore a wide range of scenarios, we chose accretion frequencies that

span both positive and negative values: [1, 1/2, 1/3, 1/10, 1/25, -1, -1/2, -1/3, -1/10, -1/25] Gyr^{-1}. As seen in Figure 7, positive values, such as 1 Gyr^{-1}, mean that the gas is mostly accreted early. Given that, as we explain below, the accretion radius grows with time, this early accretion will concentrate near the galaxy's center. Negative values, such as -1 Gyr^{-1}, indicate that gas accretes predominantly later in the galaxy's evolution, primarily in the outer regions, where the higher angular momentum contributes more significantly to the galaxy's dynamics. This range allows us to investigate different accretion scenarios and their impact on the model, providing a comprehensive understanding of how varying accretion rates affects galactic evolution.

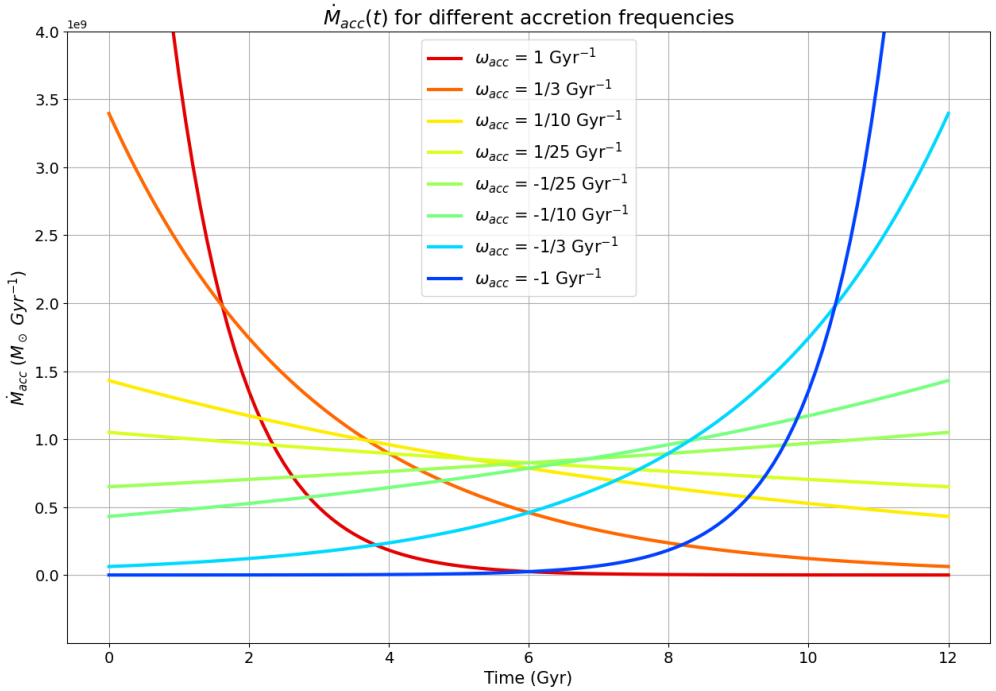

Figure 7: Gas accretion rate as a function of time (12 Gyr is the present time) for different accretion frequencies. Negative values correspond to an exponentially increasing accretion rate in time, which can sometimes happen, especially in low-mass galaxies. This is an example for a galaxy with a baryonic mass at $z = 0$ of $M_{\rm bar} = 10^{10} M_\odot$.

The gas accretion rate surface density was also taken as an exponential (but with radius), and can be described as follows:

$$\dot{\Sigma}_{\rm acc}(t, R) = \frac{\dot{\rm M}_{\rm acc}(t)}{2\pi r_{\rm acc}^2(t)} e^{-\frac{R}{r_{\rm acc}(t)}} \tag{9}$$

where $\dot{\Sigma}_{\rm acc}$ is the gas accretion rate surface density, and $r_{\rm acc}(t)$ is a radial scale length, of which we outline the derivation in Section 2.6. The latter represents the effective radius over which accreting material is distributed. The disk was taken to be exponential both radially and temporally because of two main reasons. Firstly, this assumption significantly simplifies calculations involving integrals, such as those required for

determining mass or rotation velocities (see Section 2.4). Secondly, it is physically meaningful, as the stellar light distribution in galaxy disks, when viewed face-on, is well described by exponential profiles (CFN19).

By imposing no outflows and radial motions of the gas (see Section 2.1), a particular feature of this model is that the total accreted surface density is the baryonic surface density ($\Sigma_{\rm bar}$), and therefore:

$$\Sigma_{\rm bar}(t,R) = \Sigma_{\rm acc}(t,R) = \int_0^t \dot{\Sigma}_{\rm acc}(t',R)\,dt' \tag{10}$$

The integral in equation 10 is taken from time $t = 0$ (the beginning of the galaxy formation process) to any time t, while the radius is fixed at R. In this model, the time range was taken from $t = 0$ to $t = 12$ Gyr. The choice of the latter timescale was made as we assume it as a typical timescale for the disk formation and evolution down to $z = 0$.
Equation 8 can be solved for the accreted mass at time t, which by extension, is the baryonic mass ($M_{\rm bar}$), as argued before. This yields:

$$\mathrm{M}_{\rm bar}(t) = \int_0^t Ce^{-\omega_{\rm acc}t'}\,dt' \tag{11}$$

This can be inverted to find the normalization constant C. Taking the current time as $t_0 = 12$ Gyr, C is given as:

$$\mathrm{C} = \frac{\omega_{\rm acc}\cdot \mathrm{M}_{bar}(t_0)}{1-e^{-\omega_{acc}t_0}} \tag{12}$$

where $\mathrm{M}_{\rm bar}(t_0)$ and $\omega_{\rm acc}$ can be substituted with a range of values as input. The values chosen for $\mathrm{M}_{\rm bar}$ were 50, ranging from $10^8\mathrm{M}_\odot$ to $10^{11.5}\mathrm{M}_\odot$; chosen so that a direct comparison to the observations of Mancera Piña et al. (2021b) and previous work by Camilleri (2022) can easily be made.

Finally, bringing Equations 5, 8 and 9 into 3 and 4, they become:

$$\frac{\mathrm{d}\Sigma_{\rm gas}}{\mathrm{d}t} = \frac{C}{2\pi r_{\rm acc}^2}e^{-\omega_{\rm acc}t}e^{-\frac{R}{r_{\rm acc}}} - \Sigma_{\rm rSFR} \tag{13}$$

$$\frac{\mathrm{d}\Sigma_\star}{\mathrm{d}t} = \Sigma_{\rm rSFR} \tag{14}$$

and $\Sigma_{\rm rSFR}$ depends on the star formation law used. These equations can be solved numerically, with various numerical integration methods. In this project, Equation 13 was solved numerically with a Runge-Kutta 4 method, while 14 was solved using Simpson's 1/3 method. The former was used as the differential equation in Equation 13 is not solvable analytically, while the latter was used as it is a simpler and accurate integration process.

2.4 Rotation curves

The calculation of specific angular momentum depends on first determining the rotation velocity. Thus, before calculating angular momentum, we must first derive the rotation velocity as a function of radius. In

this model, we assume two distinct yet complementary behaviors for rotation velocity. Firstly, we assume that the rotation velocity remains constant over time. This assumption simplifies the model compared to a scenario where rotation velocity changes over time. Furthermore, the primary reason for this simplification is that it makes the model self-consistent. In fact, in the absence of radial flows, gas that accretes at a certain radius remains fixed at that radius throughout the entire disk evolution. If rotation velocity were to increase with time, it would introduce additional, unphysical angular momentum. Secondly, we assume that the rotation velocity increases with radius. This radial dependence is a significant improvement over previous models because it more accurately reflects the behavior observed in real galaxies. To determine the constant value of the rotation velocity (v_{flat}) over time, we use the Baryonic Tully-Fisher Relation (BTFR) found by McGaugh (2012):

$$\mathrm{M_{bar}}(t) = A_{\rm BTFR} \cdot v_{\rm flat}^4(t) \rightarrow v_{\rm flat}(t) = \left(\frac{\mathrm{M_{bar}}(t)}{A_{\rm BTFR}}\right)^{1/4} \tag{15}$$

where $A_{\rm BTFR} = 47 \pm 6 \mathrm{M_\odot km^{-4} s^4}$ (McGaugh, 2012). While in previous works (Camilleri, 2022) this was calculated based on the baryonic mass of the disk, which changes in time, in this work the velocity was calculated according to the baryonic mass today (at $t_0 = 12$ Gyr), and this value was used throughout evolution.

Radially, the rotation curve was taken to have the following functional form:

$$v_{\rm rot}(R) = v_{\rm flat}\left[1 - \exp\left(-\frac{R}{R_v}\right)\right] \tag{16}$$

where R_v is a radial scale length that determines the initial steepness of the curve (Boissier et al., 2003), and $v_{\rm flat}$ is taken to be the value predicted by the BTFR (Equation 15). The values of R_v were determined empirically using data from the SPARC catalog (Lelli et al., 2016). The asymptotically flat rotation velocities ($v_{\rm flat}$) were obtained directly from the published table, whereas to determine the R_v values, we fitted the functional form in equation 16 to the published rotation curves for all available galaxies. Choosing the published $v_{\rm flat}$ values instead of the ones obtained from fitting was done because, while most values agreed with each other, some fitted $v_{\rm flat}$ values appeared to be slightly higher due to the fact that Equation 16 was not able to capture fully the flat part of the rotation curve (see Figure 8a). Figures 8b, 8c, and 8d show three example of rotation curves fitted with Equation 16.

2.4.1 Determination of R_v

Once all the rotation curves in the SPARC catalogue had been fitted with Equation 16, the R_v - v_{flat} relationship was first done by simply plotting all the fitted values, excluding 20 galaxies for which the fit failed (for example by having infinite error bars or that were consistent with negative values). The corresponding values of the fitted parameters can be seen in Figure 9, with R_v as a function of v_{flat}.
Figure 9 shows that there is a mild correlation between the data and the error bars are large. The data exhibited a lot of scatter, causing a correlation to be hardly found. Because of this, we decided to collect the data into 5 bins. This was done to ensure that a relationship could still be found (see Figure 10). The obtained relationship was:

$$R_v(\mathrm{kpc}) = \gamma \cdot v_{\rm flat}(\mathrm{km/s}) + \delta \tag{17}$$

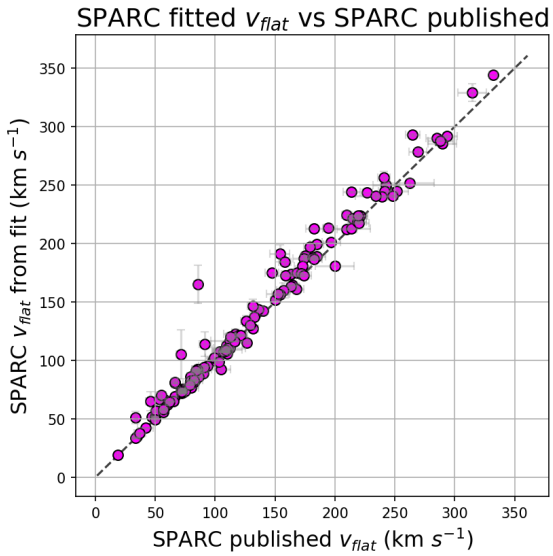

(a) v_{flat} values comparison

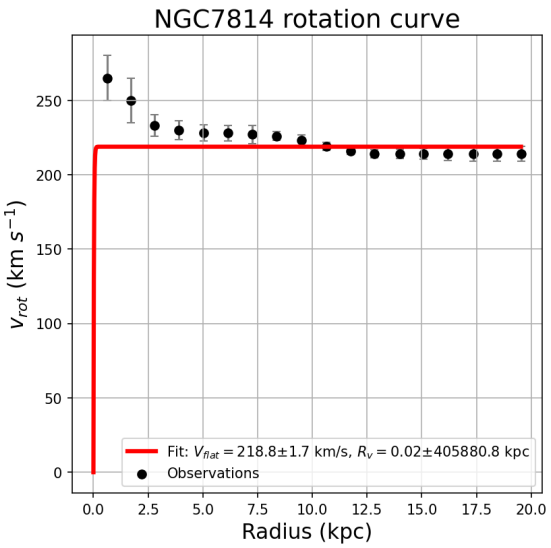

(b) NGC7814 Fit

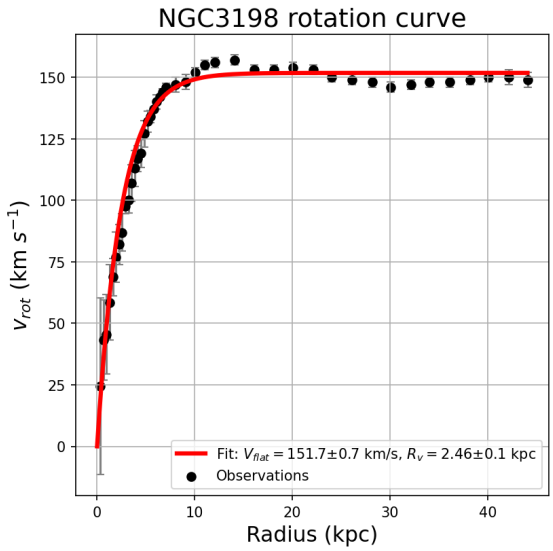

(c) NGC3198 Fit

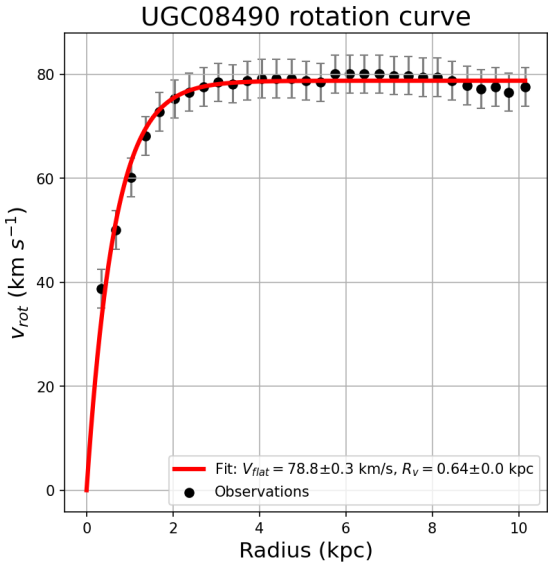

(d) UGC08490 Fit

Figure 8: Difference between fitted v_{flat} values from the SPARC catalogue with the published values and the values obtained with our fits of Equation 16 (a), and rotation curves for three example galaxies (b, c, d).

where the best fit parameters were $\gamma = -0.005 \pm 0.002 \frac{\rm kpc}{\rm km/s}$ and $\delta = 2.67 \pm 0.32$kpc.
The scatter is likely due to a combination of not perfect fitting, poor resolution in the inner parts of the galaxies, or the rotation curve not extending enough to reach convergence of $v_{\rm rot}$. As such the fitting algorithm

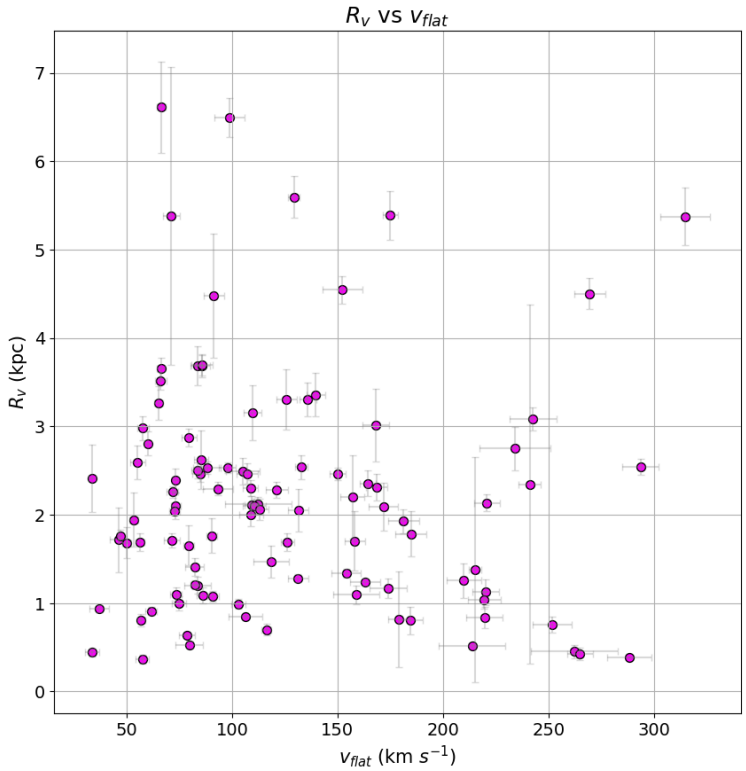

Figure 9: R_v determined from the SPARC rotation curves, as a function of asymptotically flat rotation velocities from the published SPARC catalog (Lelli et al., 2016). The figure shows the weak correlation between the data.

struggled in accurately determining the values of R_v in some galaxies. Despite the large uncertainties, we proceeded with fitting the data nonetheless because most of the galaxies had relatively well fitted parameters (see Figure 8), and because it is essential to establish a relationship between R_v and $v_{\rm flat}$ for our model. While the correlation is modest, it suffices for our purposes as one of the main objectives was to include a radial dependence on the rotation velocity. By fitting this relationship, we can improve our theoretical framework and better predict the rotational behavior of galaxies across different radii. Nonetheless, improving this fit could prove as a future improvement of the model and we discuss it in Section 4.2.2.

2.5 Specific Angular Momentum and Gas Fraction

To develop a model capable of predicting the relationship found by Mancera Piña et al. (2021b), we need to output the specific angular momentum and the fraction of gas of the galaxy. The gas fraction, $f_{\rm gas}$, is defined as the ratio between the gas mass and the total baryonic mass of the galaxy. Mathematically, as a function of time, this is defined as:

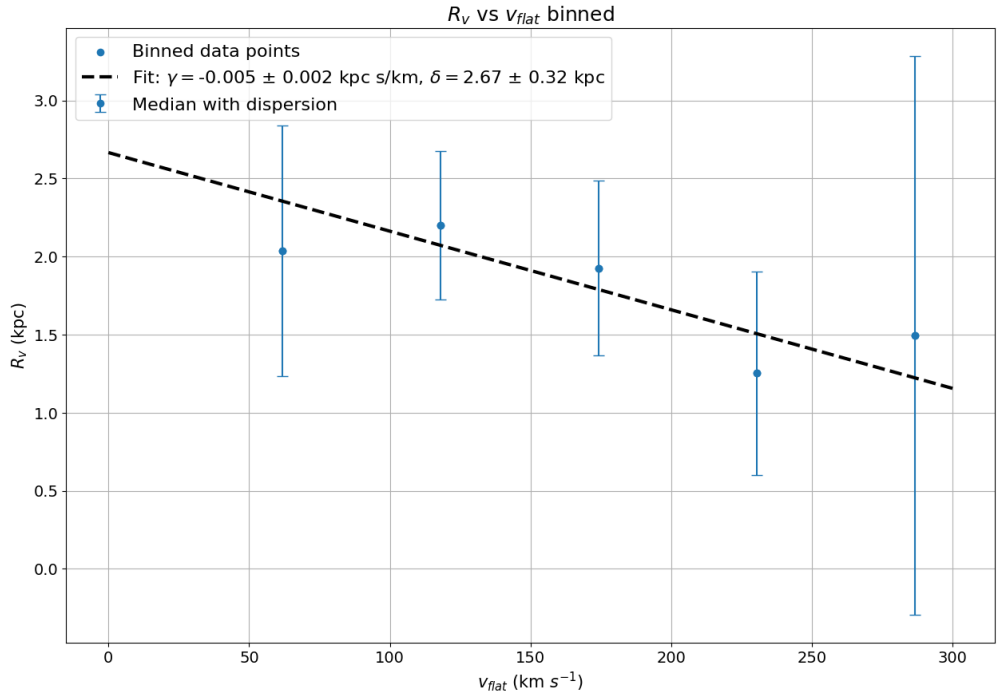

Figure 10: R_v as a function of asymptotically flat rotation velocities (Lelli et al., 2016). The values have been placed in 5 bins with their dispersion. The black dashed line shows the fit, then used in determining R_v for the purposes of the model.

$$f_{\rm gas}(t) = \frac{\mathrm{M}_{\rm gas}(t)}{\mathrm{M}_{\rm bar}(t)} \tag{18}$$

The mass, as a function of time, for any matter component of the galaxy can be determined by integrating the surface density of that component over the radius. This approach allows to calculate the total mass enclosed within a given radius R. The mass $M_i(t)$ of a component i can be expressed as:

$$\mathrm{M}_i(t) = 2\pi \int_0^{R_{\rm max}} \Sigma_i(t,R) R\, dR, \tag{19}$$

where $\Sigma_i(t,R)$ is the surface density of component i at radius R and time t. The subscript i can indicate gas, star, or baryonic components. Here $R_{\rm max}$ is the radius of the entire galaxy. This radius is determined by examining the distribution of the baryonic mass as a function of radius and identifying the point where the mass distribution converges. Doing this ensures that the integral encompasses the entire mass of the galaxy. A safely large value for this parameter was found to be $R_{\rm max} = 100$ kpc. While this is much larger than the typical radius of galaxies, especially low-mass galaxies, extending to such large radii does not significantly affect the results because it is taken as a high value precisely to ensure convergence.

The specific angular momentum is a fundamental property in galactic scaling relations, representing the angular momentum per unit mass. It is determined by weighing the local specific angular momentum j, $R \cdot v_{\rm rot}(t,R)$, by the surface density (CFN19). This is mathematically expressed as:

$$j_i(t, R < R_{\rm max}) = \frac{2\pi \int_0^{R_{\rm max}} \Sigma_i(t,R) v_{\rm rot}(t,R) R^2 \, dR}{2\pi \int_0^{R_{\rm max}} \Sigma_i(t,R) R \, dR} \tag{20}$$

, where the subscript i again represents the various components. In cases when the rotational velocity is assumed to be constant with radius (a radially flat rotation curve), the rotational velocity can be taken out of the integral. Considering all the baryons, and an exponential surface density profile of the accreting gas, as seen in Equation 9, Equation 20 reads:

$$j_{\rm acc}(t) = 2 v_{\rm rot}(t) r_{\rm acc}(t) \tag{21}$$

where $r_{\rm acc}(t)$ is scale length of accretion.
If, instead, the rotation curve follows the functional form described in Equation 16, the result of Equation 20 becomes more complex (again for the baryonic content and assuming an exponential surface density profile):

$$j_{\rm acc}(t) = \frac{2 v_{\rm flat}}{r_{\rm acc}^2} \left(r_{\rm acc}^3 - r_b^3 \right) \tag{22}$$

where $r_b = \frac{R_v r_{\rm acc}}{R_v + r_{\rm acc}}$ and R_v is determined following the relation seen in Equation 17.

For disk galaxies, the gaseous disk is usually more extended than the stellar disk. Since the angular momentum is directly proportional to the radius and the rotation tends to a constant value at large radii, gas often ends up contributing more to the angular momentum in the outer regions of the galaxy. Because of this, as gas fraction increases, the gas content becomes more significant than the stellar content, and the angular momentum increases.

2.6 Determination of $r_{\rm acc}$ from the accreting angular momentum

One of the defining properties of this model is that it describes galaxies that grow inside-out. This means that gas accreting from the CGM is deposited at progressively larger radii over time. In other words, the inner parts of the galactic disks dominate the accretion earlier in the galaxy's evolution, whereas the outer parts dominate later. This also results in the surface densities of the baryonic matter not being perfectly exponential. The inside out growth can be modeled by an increasing angular momentum, as a function of time. In this model, the accreting specific angular momentum was assumed to be as follows:

$$j_{\rm acc}(t) = j_{\rm min} + k(j_{\rm max} - j_{\rm min}) \left(\frac{t}{t_0} \right)^n \tag{23}$$

where $t_0 = 12$ Gyr, and k and n are free parameters. $j_{\rm max}$ is determined from Equation 1, imposing that the maximum angular momentum must be found in the outermost regions, where $f_{\rm gas} = 1$ (or $\log f_{\rm gas} = 0$). Therefore, $\log(j_{\rm max}(\mathrm{M_{bar}})) = 0.73 \log(\mathrm{M_{bar}}) - 4.25$. On the other hand, j_{min} was found by dividing $j_{\rm max}$ by 10. Although this choice is somewhat arbitrary, this ensures that the accretion radius is not zero, which would cause an infinite gas accretion rate surface density (see Equation 9). Lastly, k and n were both chosen to be

equal to 1 in this model, as to simplify calculations. Costa (2023) tested a limited number of combinations of these two parameters, ranging from 0.5 to 2, and the results suggested that both parameters set to 1 gave the best prediction of the observations. Changing these parameters could prove to be a further improvement of the model, when different star formation laws are also considered, and is discussed in Section 4.2.1.

Depending on whether the rotation curve is flat or not, $r_{\rm acc}$ can be determined in different ways. If the rotation curve is flat, the calculation is straightforward:

$$r_{\rm acc}(t) = \frac{j_{\rm acc}(t)}{2v_{\rm rot}} \tag{24}$$

However, if the rotation curve is not flat, then Equation 22 is more complex to invert. In this project, it was solved numerically using the Newton's method. The Newton's method is particularly well-suited for this task because it is an iterative method that converges quickly to a solution when provided with a good initial guess. This efficiency is crucial when dealing with non-linear equations where analytical results might not be feasible.

In Figure 11 we show the behavior of $r_{\rm acc}(t)$ for three example masses, comparing the rotation curve with an exponential radial dependence (Equation 16) with the flat rotation curve scenario.

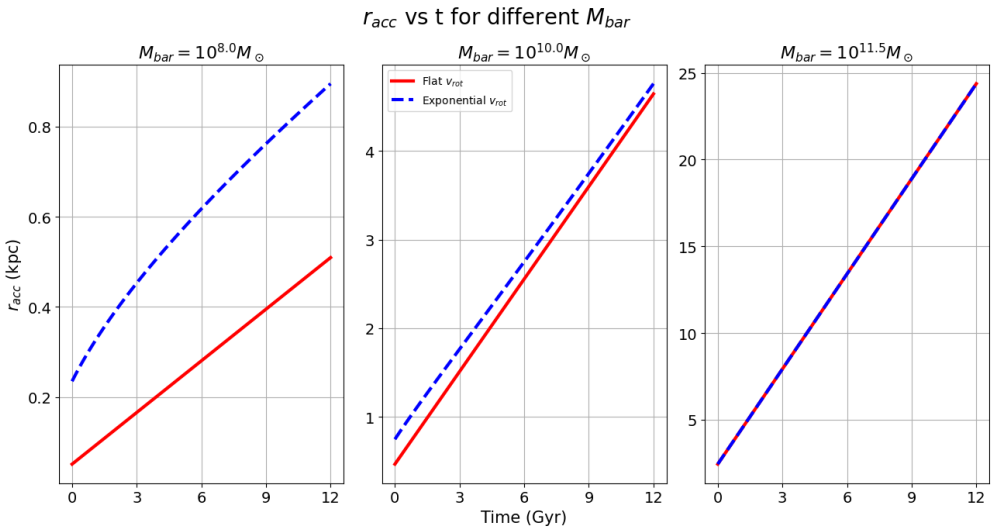

Figure 11: Accretion scale radius (r_{acc}) as a function of time for three example masses: 10^8 $M_\odot$, 10^{10} $M_\odot$, and $10^{11.5}$ $M_\odot$. In each graph we compare r_{acc} for two types of rotation curves: an exponential radial dependence (Equation 16), and a constant v_{rot}.

As can be seen from the plots, there is a clear difference between the two solutions of $r_{acc}(t)$ in the $M = 10^8$ $M_\odot$ case. Oppositely, in the case of $M = 10^{11.5}$ $M_\odot$, the two solutions appear almost identical. This behavior is caused by the fact that as the mass increases, the value of R_v decreases. Comparing Equations 21 and 22 shows that if R_v decreases, the difference between the two solutions decreases as well, with the limit that as R_v approaches 0, then Equation 22 approaches 21. For this reason, the difference is very evident

for $M = 10^8$ $M_\odot$ but not for $M = 10^{11.5}$ $M_\odot$. The implication of this difference on the model solution is a difference in the gas surface density, $\Sigma_{\rm gas}$. For lower masses, the exponential rotation curve causes a higher accretion scale length, almost twice as large. This will cause the disk to be more extended in the lower mass regimes, compared to a flat rotation curve scenario. On the other hand, for larger masses, the difference becomes less and less significant and the galaxy disk will be less impacted. This is a positive aspect of the model, because it includes the realistic feature that galaxies with lower mass have a rotation curve that rises more slowly, which implies more extended disks, and vice versa.

2.7 Analytical solution of $j_{\rm bar}(t)$

The baryonic specific angular momentum can be calculated using Equation 20 with the baryonic surface densities, or alternatively using the following equation:

$$j_{\rm bar}(t) = \frac{\int_0^t j_{\rm acc}(t') \cdot \dot{M}_{\rm bar}(t')\, dt'}{M_{\rm bar}(t)} \tag{25}$$

The analytical solution to this equation, using three example accretion frequencies ($1/3$, $1/25$, and $-1/3$ Gyr^{-1}), is shown in Figure 12.

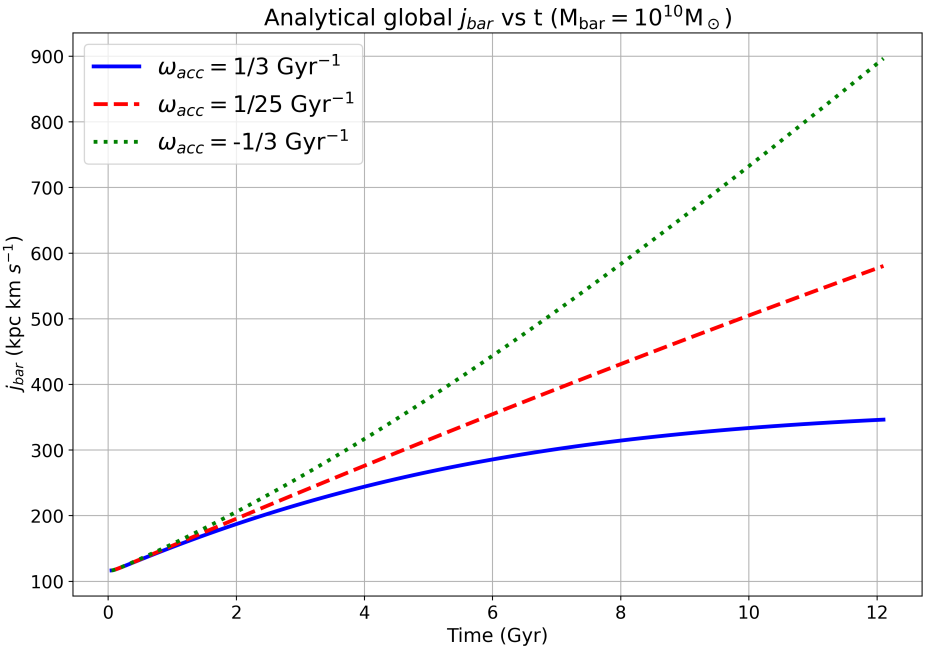

Figure 12: Specific angular momentum temporal profile. The present day baryonic mass and accretion frequency values are fixed at 10^{10} $M_\odot$ and $-1/3$ Gyr^{-1}, respectively. The results given using the three star formation laws are shown in red, green and blue.

The plot shows that the angular momentum is increasing throughout the entire galaxy evolution. In general, this conforms with the theoretical part of the model concerning inside-out growth, which has an increasing

accreting specific angular momentum at all times. More specifically, however, we can further investigate the dependence of $j_{\rm bar}$ on the accretion frequency. If the accretion frequency is positive, the gas accretion rate is exponentially decreasing, and this implies that the rate of increase in specific angular momentum decreases with time. This can be seen in the red and blue curves. On the other hand, the green line corresponds to a negative accretion frequency, therefore its steepness increases with time.

A particular note to be made regarding $j_{\rm bar}$ is that it is independent on the star formation laws. In Figure 13 the solution of $j_{\rm bar}(t)$ using the baryonic surface densities is shown, at fixed accretion frequency, comparing the results using the three star formation laws considered. We also show the analytical prediction of $j_{\rm bar}(t)$ based on the assumptions of the model. It can be clearly seen that there is no difference between the specific angular momenta when different star formation laws are used, and also the analytical solution matches the solutions using the baryonic surface densities. This latter aspect shows the numerical consistency of the model.

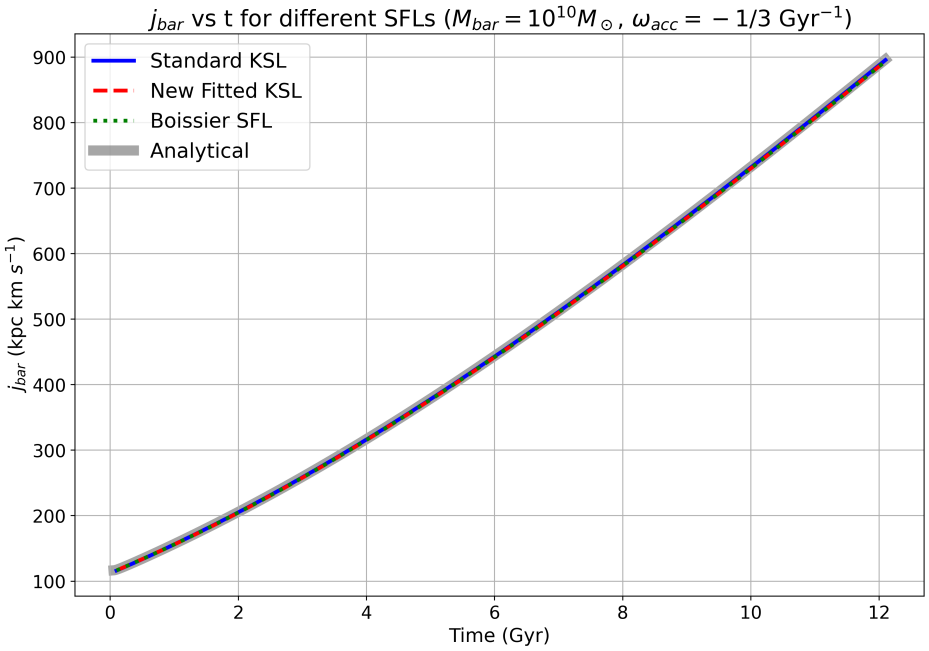

Figure 13: Comparison of the specific angular momentum obtained from the baryonic surface density profiles, for different star formation laws and the analytical solution. The present day baryonic mass and accretion frequency values are fixed at 10^{10} M$_\odot$ and $-1/3$ Gyr^{-1}, respectively. The results given using the three star formation laws are shown in red, green and blue, while the analytical solution is shown with a less opaque and larger grey line.

3 Results

In this chapter, we apply the methods described above to explore three different models, each utilizing a different star formation law, and present the main results for each. We begin by discussing the main properties of the models (Section 3.1), including the surface density profiles, the global mass evolutions, and the gas fraction and specific angular momentum evolution. For illustrative purposes, we will focus on a single value of $\mathrm{M_{bar}}(t_0) = 10^{10}\mathrm{M}_\odot$. Then, we confront the surface density profiles with observations; we will do this for a single galaxy (NGC2403) for illustrative purposes. Following this, in Section 3.3 we explore the predictions of the models for the $j_{\rm bar} - \mathrm{M_{bar}} - f_{\rm gas}$ relation, comparing the results with observational data from Mancera Piña et al. (2021b).

3.1 Disk Evolution Model

3.1.1 Surface Density Profiles

The first step is to investigate the evolution with time of the surface density profiles for gas and stellar components. These profiles were calculated using Equations 13 and 14, assuming different star formation laws (see Section 2.2). In Figure 14 we illustrate the gas surface density ($\Sigma_{\rm gas}$) profiles as functions of radius at various times, using the Boissier law and comparing three accretion frequencies that are representative of our chosen range: $\omega_{\rm acc} = 1/3$, $1/25$, and $-1/3$ Gyr^{-1}.

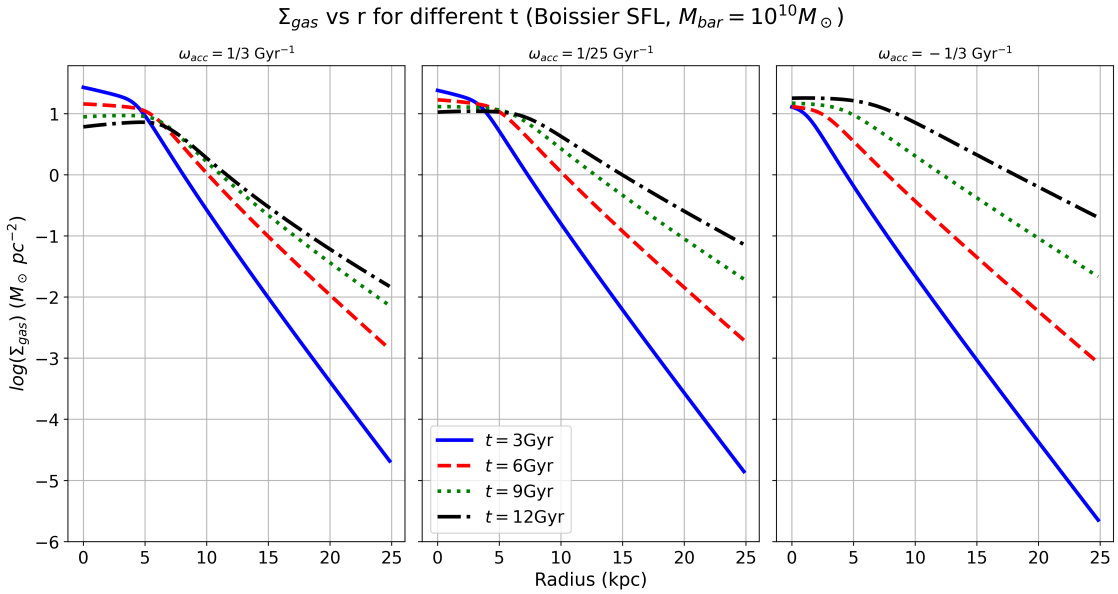

Figure 14: Gas surface density as a function of radius at four times, 12 Gyr being the present time, using our fit for the Boissier SFL and $\mathrm{M_{bar}}(t_0) = 10^{10}\mathrm{M}_\odot$. The accretion frequency was varied using three values: $1/3$ (left), $1/25$ (center), and $-1/3$ Gyr^{-1} (right).

As can be seen from the plots in Figure 14, the gas surface density decreases with radius for all accretion

frequencies, except in a small inner region at later times. Notably, the surface density is higher in the inner regions for earlier times (blue line) compared to later times (black line), when a positive accretion frequency is considered. Conversely, in the outer regions of the galaxy, the surface density increases with time for all accretion frequencies. This behavior is a consequence of the inside-out growth assumption: the gas accretes at progressively larger radii over time, which increases the surface density as we move away from the galactic center. Meanwhile, for a positive accretion frequency (left and center plots), near the core the gas has already mostly accreted at early times, after which it is being used by star formation but not being replenished. This leads to a decrease in gas surface density over time in the inner regions when the accretion history is characterized by a high and positive accretion frequency (higher values result in a more significant decrease of $\Sigma_{\rm gas}$ over time). In contrast, negative accretion frequencies (right plot) show an interesting trend where gas accretion increases exponentially with time at all radii. This can be understood by considering that during the early stages of galaxy evolution, there is scant gas accretion across all radii, leading to low initial gas surface densities. However, as time progresses, the accretion rate accelerates significantly. When combined with the inside-out growth mechanism, where gas accretes at progressively larger radii over time, this means that the inner regions start with minimal gas available for star formation. Over time, as more gas is accreted, it primarily accumulates in the outer regions, leading to a gradual increase in gas surface density across all radii. This delayed but substantial accretion in the later stages ensures a continuous increase in gas surface density over time at all radii.

Figure 15 presents the gas surface density ($\Sigma_{\rm gas}$) profiles as functions of radius at various times, and employing different SFLs, for a value of $\omega_{\rm acc} = 1/25$ Gyr^{-1} and a final baryonic mass of $M_{bar}(t_0) = 10^{10}$M$_\odot$. $\omega_{\rm acc} = 1/25$ Gyr^{-1} was chosen as it represents an intermediate value among those explored in the models (see Figure 7).
As can be seen from the plots in Figure 15, differences between the gas surface densities using different star formation laws can be noticed particularly in the inner regions. In fact, there seems to be a change in slope beyond roughly 8 kpc for both our KS and Boissier law fits, increasing in steepness. This change in slope can be explained by examining the behavior of the star formation rate surface density as a function of the gas surface density, as seen in Figure 6. In the inner regions, where the gas surface density is higher ($\gtrsim 10$ M$_\odot$pc^{-2}), the standard KS law predicts a lower SFR, according to the data. Because of this, for the other two laws the model might turn a considerable amount of gas into stars in the inner regions of the galaxy, resulting in the observed shallower slope compared to the outer regions.

Due to the much steeper dependency of the star formation rate on gas surface density for our fits of the KS and Boissier laws, compared to the standard KS law the star formation rate surface density becomes significantly lower at larger radii, which correspond to small gas surface densities. For the Boissier law, this is influenced not only by the steep slope but also by the inclusion of the angular velocity, Ω, which further reduces the star formation rate in the outer regions. This effect is evident in Figure 16, where the star formation rate surface density at larger radii drops to levels significantly lower than the minimum observed values of $\Sigma_{\rm SFR}$ in the data used (see Figure 6).
A first note in Figure 16 can be made concerning the baryonic surface density, $\Sigma_{\rm bar}$ (third panel row): the profiles are not perfect exponentials. This is related to the fact that $r_{\rm acc}$ is not a constant and depends on time. Specifically, the inside-out assumption implies that gas accretes at progressively larger radii over time, increasing the value of $r_{\rm acc}$ (Figure 11) and causing a curved $\log(\Sigma_{\rm bar})$ profile. Another observation is that

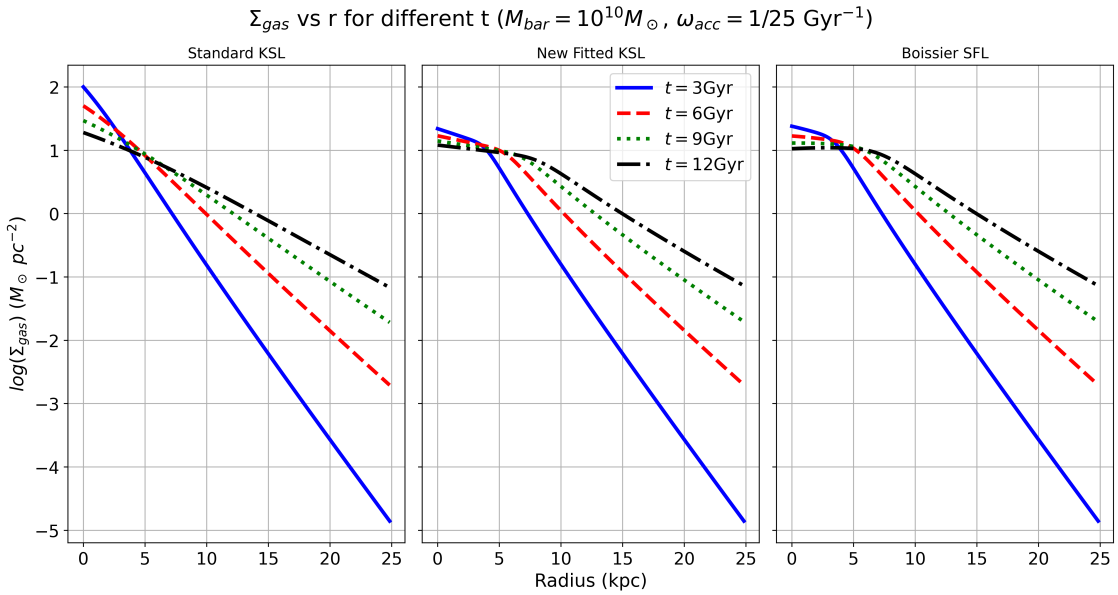

Figure 15: Gas surface density as a function of radius at four times, 12 Gyr being the present time, for a model with $\omega_{\rm acc} = 1/25$ Gyr^{-1} and $M_{bar}(t_0) = 10^{10}$M$_\odot$. Three different star formation laws were considered: the standard KS law (left), the version of the KS law with our fit (center), and the Boissier law (right). The plots show the radial profiles at four times during the evolution.

$\Sigma_{\rm bar}$ is independent on the star formation law. These are consequences of our assumption; we show these profiles here for clarity and as a validation of the model's performance.

The first panel row shows the evolution of the $\Sigma_{\rm SFR}$ radial profiles for the three star formation laws considered. It is clear that the predicted SFR is much lower, compared to the standard KS law, for the KS and Boissier law fits at large radii, and in particular the KS law fit, which has a steep slope of 3.83 (see Section 2.2.3). A lower $\Sigma_{\rm SFR}$ results in a lower $\Sigma_\star$, which can be seen in the second panel row. To assess the quality and realism of these theoretical predictions, we will compare them, along with the gas surface density, with real galaxy observations in Section 3.2.

3.1.2 Evolution of $M_{\rm gas}$, $M_{\rm SFR}$, and $M_\star$

After obtaining the surface densities, we subsequently calculate the temporal evolution of the global galaxy mass of gas and stars, following the method described in Section 2.3. In Figure 17 we show the gas, SFR, and stellar mass as a function of time, assuming again a present day baryonic mass of 10^{10}M$_\odot$, and comparing the results for the three SFLs and three different values of the accretion frequency.
As expected, varying the star formation law induces differences in the evolution of the global gas mass. The most visible differences can be seen for an accretion frequency of $\omega_{\rm acc} = 1/3$ Gyr^{-1} (top left panel in Figure 17). For this value of $\omega_{\rm acc}$, the evolution of $M_{\rm gas}(t)$ is characterized, for all three star formation laws, by an initial growth, followed by a peak, and then a decline. When using the standard KS law, the gas mass exhibits

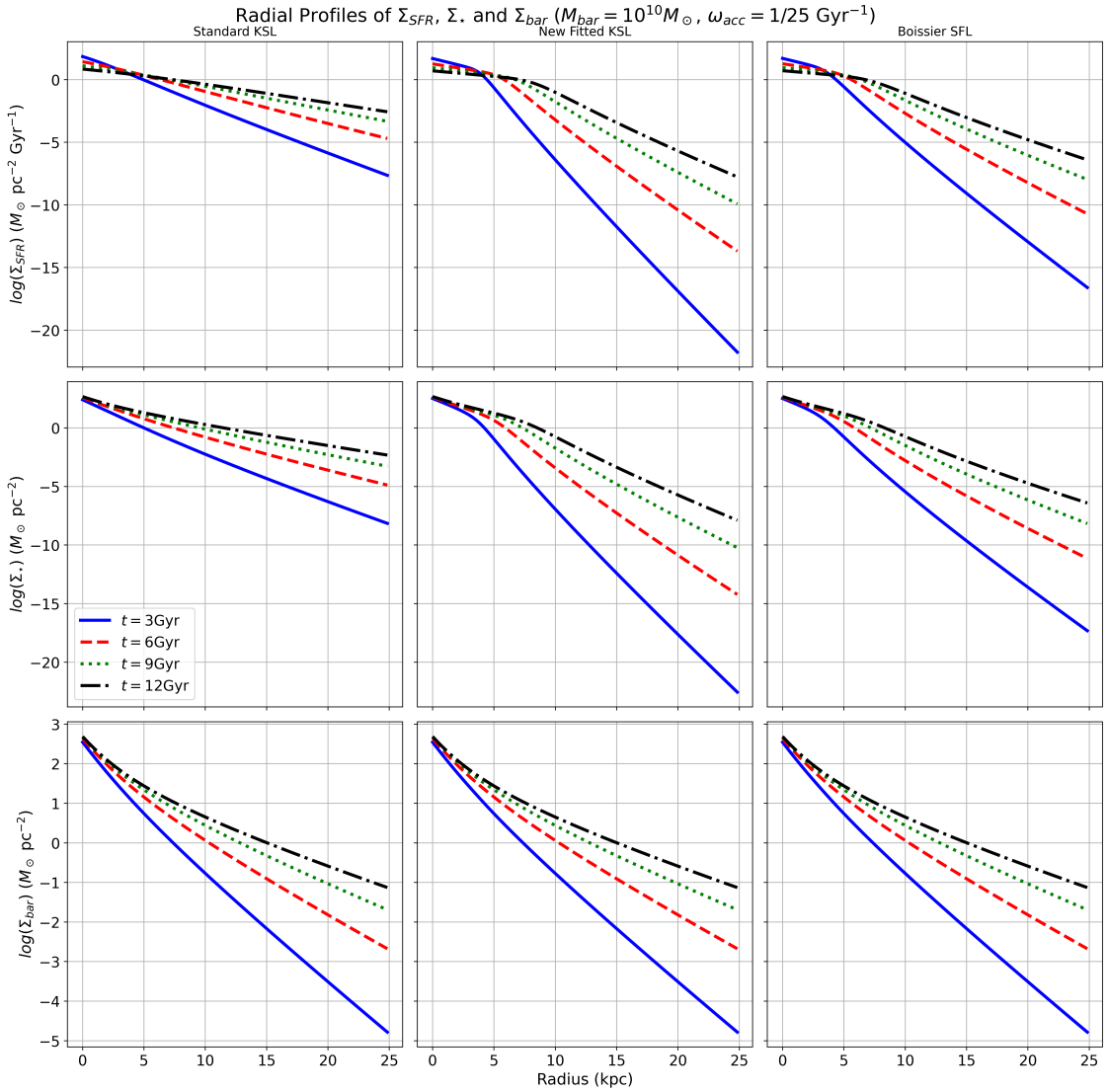

Figure 16: Radial profiles of star formation rate (top row), stellar mass (middle row), and baryonic mass (bottom row) surface densities for the same models as those presented in Figure 15. The three star formation laws are presented in each column.

a significantly higher peak compared to the cases when the other two star formation laws, the new fitted KS law and the Boissier law, are assumed. Furthermore, the peak also occurs earlier in the evolution. This can be explained by considering that for high, positive accretion frequencies, most of the gas is accreted early in the evolution. This causes a peak in the gas mass, which later decreases as less gas is accreted and star formation dominates. For an accretion frequency of $\omega_{\rm acc} = 1/25$ Gyr^{-1}, this is less significant because the gas accretion rate decreases more slowly (see Figure 7), resulting in a more sustained replenishment of the gas reservoir. Consequently, the overall present day global gas mass is higher compared to the $\omega_{\rm acc} = 1/3$

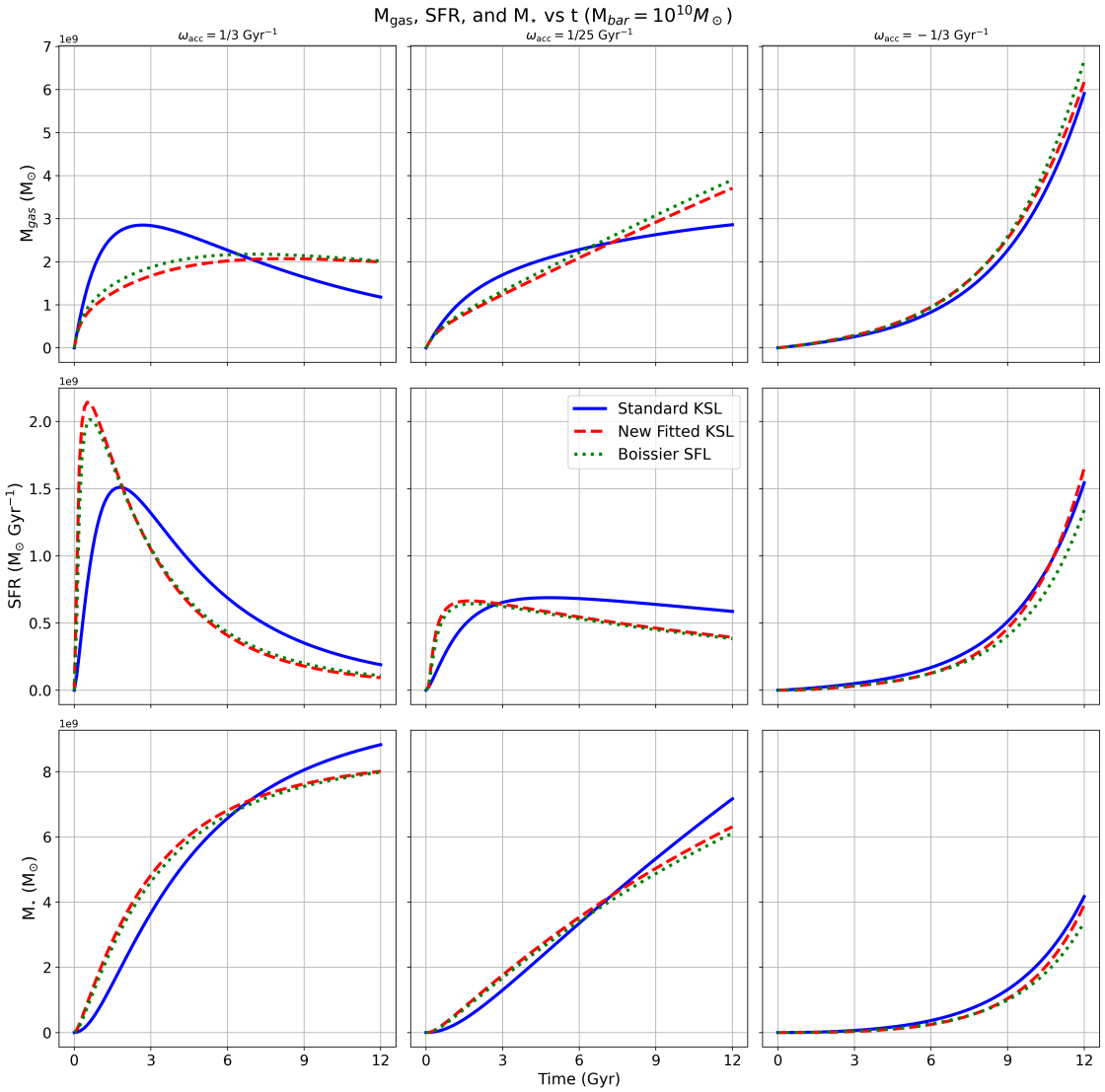

Figure 17: Temporal profiles of the global gas mass (top row), SFR (middle row), and stellar mass (bottom row). The present day baryonic mass is fixed at 10^{10} $M_\odot$, while the accretion frequency is varied: $1/3$ (left), $1/25$ (middle), and $-1/3$ Gyr^{-1} (right).

Gyr^{-1} case, where the gas is depleted more rapidly. In the case of a negative accretion frequency, on the other hand, the gas accretion rate increases exponentially, which causes the gas mass to also increase with time.

In Figure 17 we can also see the evolutions of the SFR and stellar mass for different star formation laws. Using the new fits of the KS and Boissier laws, there is a higher peak in SFR in the very early stages of the evolution when an accretion frequency of $\omega_{\rm acc} = 1/3$ Gyr^{-1} is considered. This is less significant in the $\omega_{\rm acc} = 1/25$ Gyr^{-1} case, for the same reasons explained before for $\mathrm{M_{gas}}$. Again, we see an increase in SFR

for negative accretion frequencies as more gas is continuously accreted over time. The global stellar mass shows a monotonic increase over time, with its growth rate determined by the shape of the SFR curves.

3.1.3 Evolution of $f_{\rm gas}$

After investigating the behavior of the surface densities and global masses, the next step is to analyze how the model is able to predict the values of $f_{gas}(t)$. In Figure 18 the values of the gas fraction are shown, at the fixed baryonic mass of $10^{10}\mathrm{M}_{\odot}$, for different SFLs and accretion frequencies.

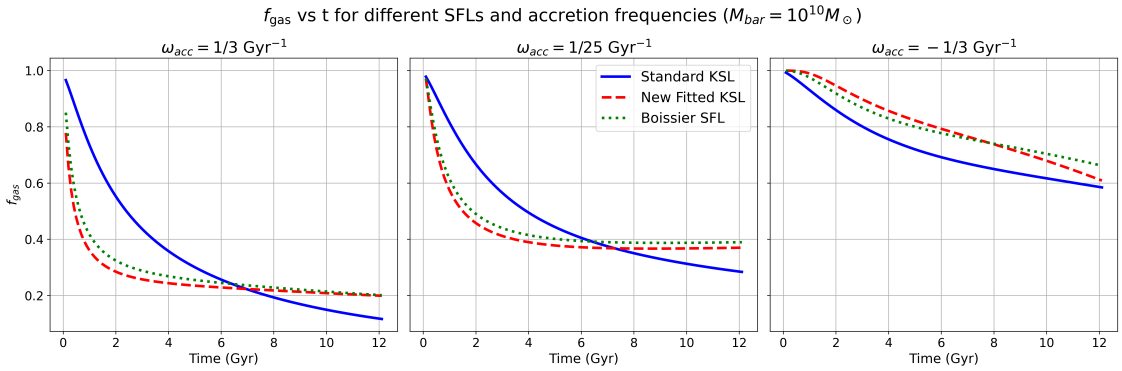

Figure 18: Global gas fraction values as a function of time for different star formation laws. The present day baryonic mass value is fixed at $10^{10}\mathrm{M}_{\odot}$, while the accretion frequency is changed using the usual three values: $1/3$ (left), $1/25$ (middle), and $-1/3$ Gyr^{-1} (right).

It can be seen that the gas fraction evolves in a different fashion if different star formation laws are employed. In particular, an interesting behavior is that for positive accretion frequencies the standard KS law predicts for most of the evolution a higher gas fraction than the other two SFLs. Despite this, beyond $t \simeq 7$ Gyr, the gas fraction given with the standard KS law decreases below the other two laws. The reasoning behind this can be explained taking into account both gas accretion and inside-out growth. In the earlier times, gas accretes near the core of the galaxy, where there is a high gas surface density. The standard KS law turns less gas into stars at high $\Sigma_{\rm gas}$ compared to the other SFLs, causing a higher gas fraction. However, as time progresses, the galaxy grows inside-out and gas starts accreting at larger radii. In this regime, the standard KS law takes over, as it turns more gas into stars than the other two laws (see Figure 6a), returning a lower gas fraction.

Contrary to the positive accretion frequency scenarios, with a negative accretion frequency the new KS and Boissier laws predict a higher gas fraction throughout the evolution. This is because as gas accretion increases exponentially with time, there is a smaller amount of gas earlier, compared to later in time. While the baryonic mass increases continuously with time, the gas surface density still decreases in the outer regions of the galaxy, therefore resulting in a higher gas fraction near the end of the evolution (see top right panel in Figure 17).

3.2 Comparison with Observed Surface Density Profiles

After analyzing the theoretical aspects of the model, it then becomes interesting to test the model predictions with observations of surface density profiles. In Figure 19 we show the baryonic surface density observations of NGC2403.

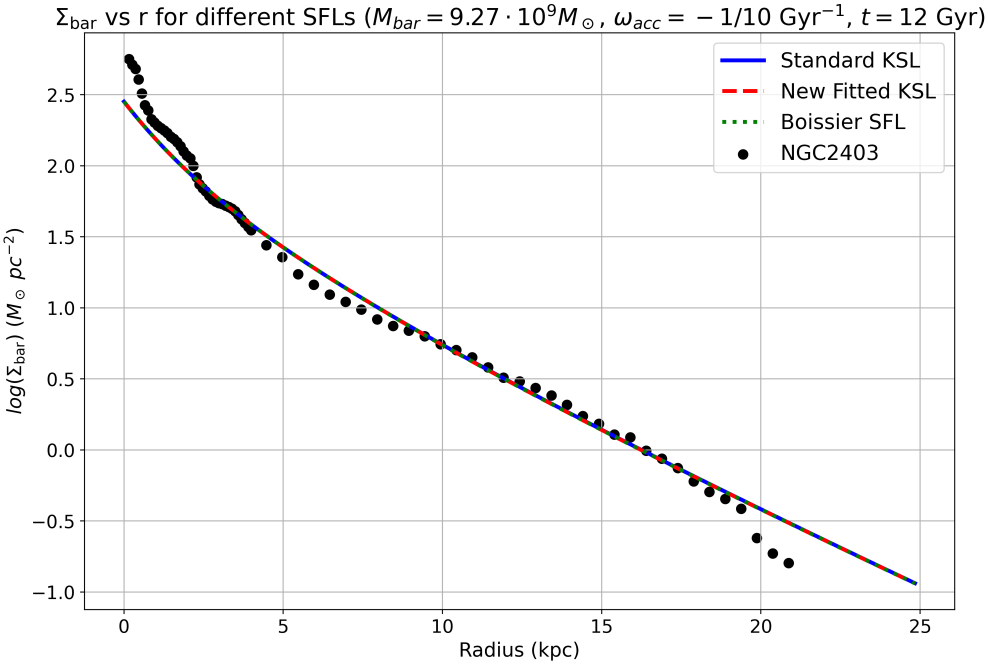

Figure 19: Comparison of the present-day baryonic surface density profiles obtained using the three star formation laws, with observations of galaxy NGC2403. The mass and accretion frequency were chosen as to match the values of the corresponding galaxy.

For this galaxy the value of the present day baryonic mass was taken from the published table by Mancera Piña et al. (2021b), whereas the value of the accretion frequency was chosen by looking at which value gave the closest present day gas fraction, again compared to the one reported in the published data by Mancera Piña et al. (2021b). This value was also checked by looking at model-data comparison of the baryonic surface density. The overlap of the curves seen in Figure 19 are expected, because the choice of star formation law should not impact the baryonic surface density, it only regulates the amount of gas turned into stars. Because of this, this plot provides a confirmation that the model is working correctly. The fact that the observed points closely match the model predictions makes this galaxy a perfect example to further explore the differences between our models.

In Figure 20 we show, analogously to Figure 19 for $\Sigma_{\rm bar}$, the radial profiles of $\Sigma_{\rm gas}$ and $\Sigma_\star$, with an accretion frequency $\omega_{\rm acc} = -1/10$ Gyr^{-1}, compared with the example galaxy NGC2403 data.
As can be seen in Figure 20a, it is clear that the new KS and Boissier laws fit to a much better degree the gas surface density, compared to the standard KS law. In the inner region ($r < 5$ kpc), both laws predict

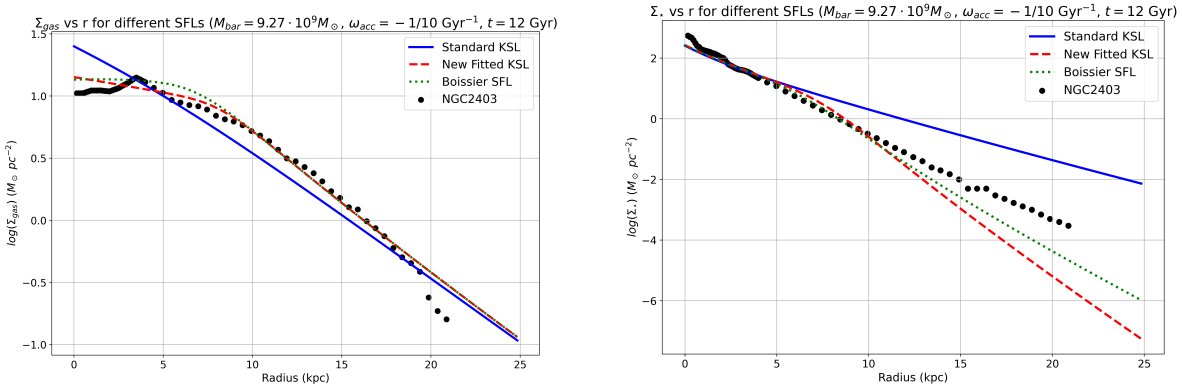

(a) $\Sigma_{\rm gas}$ (b) $\Sigma_\star$

Figure 20: Comparison of the present-day gas and stellar surface density profiles obtained using the three star formation laws, with observations of the galaxy NGC2403.

a flattening of the surface density profile which is also observed in NGC2403. In contrast, the standard KS law (blue line) predicts a gas surface density that is almost three times higher than the one observed in NGC2403, in the inner regions. Beyond 5 kpc, the standard KS law predicts, instead, a lower gas surface density compared to observations, whilst the two other star formation laws both predict very well the trend observed.
Moving to the outermost regions of the galaxy ($r \gtrsim 20$ kpc) the gas surface density from all three star formation laws seems to converge to a higher value than the one observed. It is important to point out that in this region there are only three data points. This convergence could be due to the fact that at larger radii the star formation efficiency is lower than in the inner regions. At large radii a negligible fraction of the accreted gas is turned into stars; this causes the profile of $\Sigma_{\rm gas}$ to tend towards the profile of $\Sigma_{\rm bar}$, which by construction is independent on SFL.

In Figure 20b the results for the stellar surface density are also compared to observations. In the inner regions the stellar surface density is very similar for all star formation laws. This follows the same argument outlined before: for all SFLs most of the accreted gas is turned into stars in the inner regions, implying that the stellar surface density profile coincides with the baryonic surface density profile (which is independent on SFL). The $\Sigma_\star$ given from the standard KS law is higher than observations beyond 5 kpc. On the other hand, the other two star formation laws predict lower values beyond 10 kpc. In general, however, in comparison with the observations the stellar surface densities using the new star formation laws (KS and Boissier) are in better agreement than the standard KS law.

3.3 The $j_{\rm bar} - {\rm M}_{\rm bar} - f_{\rm gas}$ Relation

In this section, we extend the application of our methodology and model to span a wide range of present day baryonic masses and accretion frequencies. The chosen mass range allows for a direct comparison with observations by Mancera Piña et al. (2021b), enabling us to investigate how the model performs in different

mass regimes (see Section 2.3). Furthermore, by varying the accretion frequencies, we aim to explore the range of specific angular momenta (j_{bar}) the model can predict. As explained in the methodology, adjusting ω_{acc} allows us to examine how j_{bar} evolves over time. The three models, each employing a different star formation law, enable us to investigate the predicted gas fractions (f_{gas}) as a function of baryonic mass (M_{bar}) and specific angular momentum (j_{bar}). We show how the final result is dependent on the star formation law, while simultaneously comparing with the observations to gain insight into which model better fits the data.

The results of the model when the star formation law is changed can be seen in Figure 21. Each sub-figure shows the results with a different star formation law: the standard KS law (a), the version of the KS law using our fit (b), and the Boissier law using our fit (c).
For each graph, 50 present-day baryonic masses were considered ($\log \mathrm{M_{bar}}/\mathrm{M_\odot}$ in a range $8-11.5$), and for each mass, 10 models were computed using the values of ω_{acc} as described in Section 2.3. The lines of constant f_{gas} have been obtained by interpolating over the predicted f_{gas} values, which correspond to different accretion frequencies used. In a general qualitative examination of the results, we can again observe that a high and positive accretion frequency results in a low gas fraction (color-coded with redder colors), while a high and negative accretion frequency returns much higher gas fractions (bluer colors), as seen previously in Section 3.1.3 and Figure 18.

All the results show that, for a constant gas fraction, the specific angular momentum, j_{bar}, increases as a function of the baryonic mass, M_{bar}. This is consistent with the observations, and is also similar to the results from previous work (see Camilleri (2022) and Costa (2023), although Camilleri (2022) did not interpolate at constant f_{gas}; see Figure 4). Comparing the models with the observational data, the values of the angular momentum for all star formation laws, show a good qualitative and quantitative agreement. Furthermore, the values of the gas fraction are also in agreement with the observations, however this is more significant for some star formation laws than others.

In general, our results show that there is little difference in the predicted $j_{bar} - \mathrm{M_{bar}} - f_{gas}$ relation when different star formation laws are used; in particular the results using the two forms of the KS law. In comparison, the results found by Camilleri (2022) (as seen in Figure 4), showed a clear difference when changing the star formation law. This could be a consequence of implementing the inside-out growth assumption into the model, which was not taken into account by Camilleri (2022), and the implications are further discussed in Section 4.1.

3.4 The $j_{bar} - f_{gas}$ Relation at Fixed Baryonic Mass

In this section we analyze the relationship between j_{bar} and f_{gas} at fixed baryonic mass. In Figure 22 we show this relationship for three present-day baryonic masses that were chosen to be representative of our range of values: 10^9, 10^{10}, and 10^{11} $\mathrm{M_\odot}$. In each plot we also show the observations by Mancera Piña et al. (2021b) of galaxies which have similar masses (galaxies were selected within a range of 0.2 dex). For the 10^{11} $\mathrm{M_\odot}$ plot we also show the HIX (HI-extreme, Mancera Piña et al. (2021b)) galaxies that have masses within the chosen range.
As seen in Figure 22b, the j_{bar} range predicted by the models with a fixed mass of 10^{10} $\mathrm{M_\odot}$ is in agreement with the observations. In this plot, all the data points are within or at the edges of the predicted j_{bar} range.

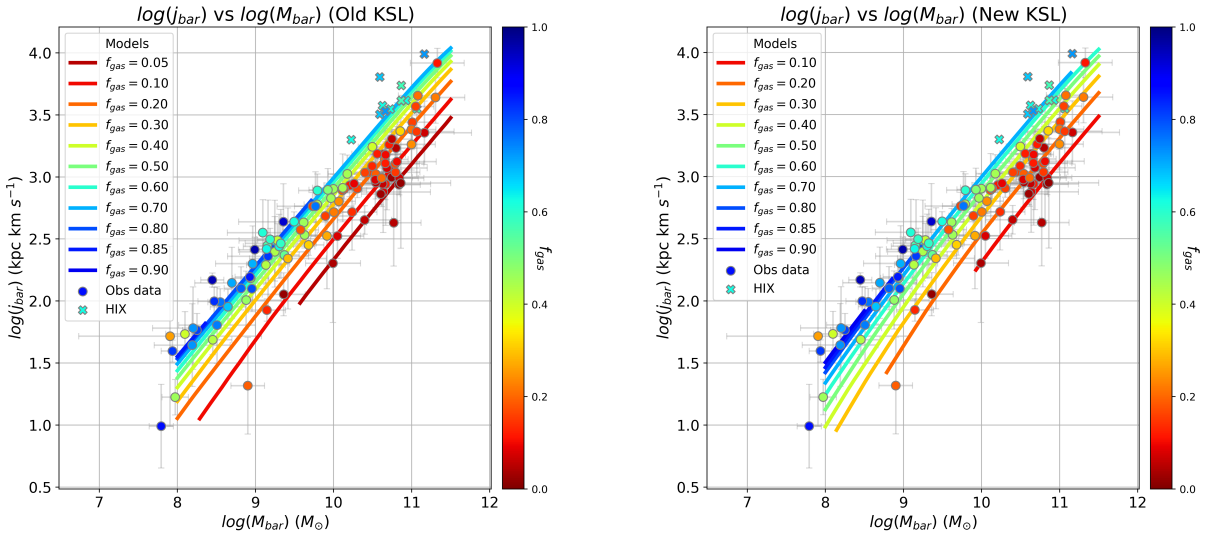

(a) Standard KS Law

(b) New Fitted KS Law

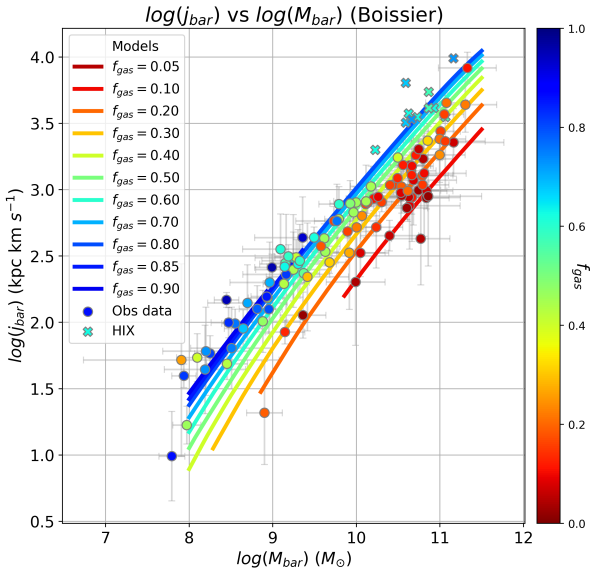

(c) Boissier SFL

Figure 21: Comparison between observations and predictions of our models for the $j_{\rm bar} - {\rm M_{bar}} - f_{\rm gas}$ relationship, using three star formation laws: standard KS law (a), new KS law (b), Boissier SF law (c). On each plot the observations by Mancera Piña et al. (2021b) are shown, as well as the lines of constant f_{gas} predicted by the models (both color coded according to f_{gas}).

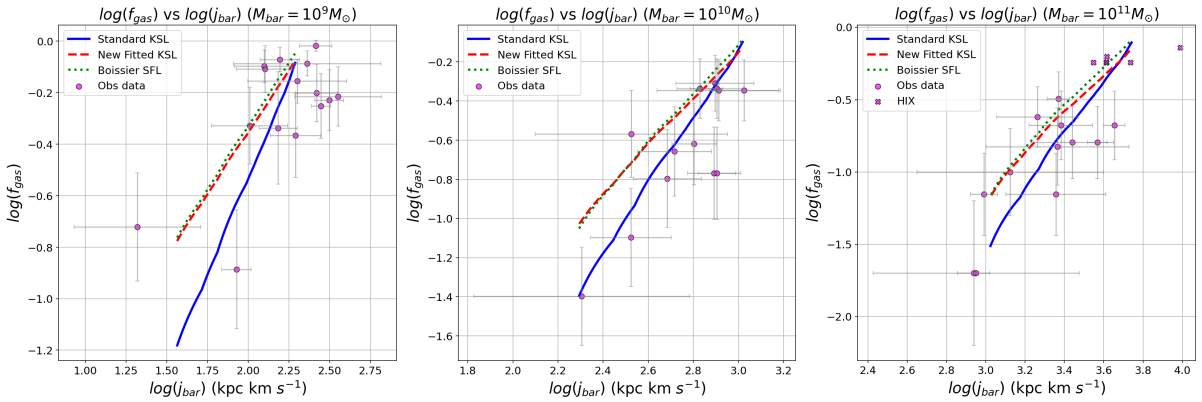

(a) $M_{\rm bar} = 10^9 M_\odot$ (b) $M_{\rm bar} = 10^{10} M_\odot$ (c) $M_{\rm bar} = 10^{11} M_\odot$

Figure 22: $\log f_{\rm gas}$ versus $\log j_{\rm bar}$ for three fixed present-day baryonic masses (10^9 (a), 10^{10} (b), and 10^{11} (c) $M_\odot$).

There are four galaxies in the 10^{11} $M_\odot$ plot (Figure 22c) that are outside of the predicted range: one of these is an HIX galaxy (with no error bar), while the rest have large error bars that fall within 1.5σ of the predicted range. Still, most other galaxies are within the obtained $j_{\rm bar}$ range. For the 10^9 $M_\odot$ plot (Figure 22a), on the other hand, several galaxies fall outside of the predicted $j_{\rm bar}$ range. All the plots in Figure 22 again show no difference in the predicted $j_{\rm bar}$ range when different star formation laws are assumed, as discussed previously.

An aspect that stands out immediately from the plots is that the standard KS law predicts lower (~ 0.4 dex) present-day gas fractions for fixed $M_{\rm bar}$ and $j_{\rm bar}$, in all mass regimes. This is more in agreement with observations in the higher-mass regime, such as with a mass of 10^{10} or 10^{11} $M_\odot$. However, for lower masses such as $M_{\rm bar} \lesssim 10^9 M_\odot$, there are too few data points to draw a conclusion on which star formation law predicts the better $f_{\rm gas}$ range. A possible interpretation of these results will be given in Section 4.1. In general, however, the standard KS law is able to predict a larger range of gas fractions, particularly by predicting the presence of galaxies with low $f_{\rm gas}$. This is evident in the regime of $\log(j_{\rm bar}) \approx 1.5 - 3$. It is important to note, however, that this conclusion is based on a limited number of observational points — two in the central (b) panel and two in the right (c) panel. While these points are still significant, the sample size is not overwhelmingly large.

The difference between the gas fractions using the two forms of the KS law decreases as the mass increases. The results obtained using the Boissier star formation law show that in all mass regimes the range of $j_{\rm bar}$ and $f_{\rm gas}$ values are relatively similar to those produced by our fit of the KS law. Still, the results show that higher gas fractions, compared to the other forms of the KS law, are obtained throughout the $j_{\rm bar}$ range for all present-day baryonic masses. In the high-mass, high-$j_{\rm bar}$ regime ($M_{\rm bar} = 10^{11} M_\odot$, $j_{\rm bar} \simeq 10^{3.6}$ kpc km s^{-1}) there are galaxies, labeled as HIX (HI-extreme, Mancera Piña et al. (2021b)), which have gas fractions of ~ 0.7. The results suggest that these galaxies are equally well predicted by all the star formation laws considered. In general, the results suggest that there is little impact of applying the different star formation

laws we considered on the prediction of the $j_{\rm bar} - f_{\rm gas}$ relation at fixed baryonic mass. The implications of this are discussed in Section 4.1.

4 Discussion

In this chapter we discuss the implications our findings and comparisons with previous works (Section 4.1), as well as the limitations and possible future work (Section 4.2).

4.1 Implications of the Results and Comparisons with Other Works

The results of our analysis of the $j_{bar} - M_{bar} - f_{gas}$ relation and its dependence on the star formation laws used were presented in Sections 3.3 and 3.4. When examining the general predictions of the model, we can conclude that the star formation law has little impact on the $j_{bar} - M_{bar} - f_{gas}$ relation. Instead, the more important ingredient appears to be the assumption of inside-out growth. This is a notable result, especially compared to previous work, such as that by Camilleri (2022), which found a strong dependence on the choice of the star formation law (see Figure 4).

Previous work already supported the inside-out growth paradigm, through the accretion of gas that has an increasing angular momentum (Costa, 2023). The minimal dependence on the star formation law, as seen in our results, reinforces the idea that the inside-out growth mechanism is a significant and crucial aspect of the model, which can also be noticed comparing the results by Camilleri (2022) and Costa (2023) (Figures 4 and 5, respectively). The observed significant increase in j_{bar} with higher f_{gas} at fixed M_{bar} also suggests that the inside-out growth framework gives better predictions when compared to observations (Figure 22).
An interesting point can be raised about the role of inside-out growth in reducing the sensitivity of the models to variations in the steepness of the star formation laws. Comparing our results from this work or previous work (Costa, 2023) with the work by Camilleri (2022), a noticeable difference can be seen in the dependence of f_{gas} on the baryonic specific angular momentum, at fixed M_{bar} and SFL. In Figure 4a it can be seen that the variation of f_{gas} with j_{bar} is rather small (a range of f_{gas} values of $0.13 - 0.43$). On the other hand, this work and previous works (Costa, 2023) which employed inside-out growth demonstrated a larger variation in f_{gas} values. This suggests that inside-out growth introduces a more varied response of the gas fraction when changing j_{bar}.
In addition, the results obtained by Camilleri (2022) also showed a larger dependence of gas fraction on the slope of a star formation law like the KS law. In Figure 4 it can be seen that at fixed M_{bar} and j_{bar}, changing the star formation law has a significant impact on the value of the gas fraction. As an example, at fixed $M_{bar} = 10^8 M_\odot$, the model that returned the highest j_{bar} value ($\sim 10^{1.7}$kpc km s^{-1}) had a value of f_{gas} of 0.43 using the KS law, or > 0.9 using the law from Gatto et al. (2013). Instead, our models showed a smaller variation in f_{gas} at fixed M_{bar} and j_{bar} when the SFL was changed, particularly for large masses and baryonic specific angular momenta (see Figure 22).

The results using the three star formation laws at a fixed mass (as seen in Figure 22) showed that the standard KS law predicted a wider range of gas fraction values across all mass regimes within our selected range. Notably, it predicted lower gas fractions for lower baryonic specific angular momentum (i.e. when high and positive accretion frequencies were used). While there are some galaxies observed with such low gas fractions, the number of these observations is limited. Therefore, we cannot definitively conclude that the standard KS law is more accurate in these regimes. To reach clearer conclusions, then, it would be necessary to obtain more observational data of galaxies with low gas fractions and low baryonic specific angular momentum

across different mass regimes. The j_{bar} range of our new models, compared with that of the Costa (2023) model, was found to be slightly lower (see Figure 23). This leaves more unexplained observational data in the high-j_{bar} regime (for all present-day baryonic masses considered), and in theory it should be independent of the star formation law. Instead, it is likely caused by the other improvements done on the model (namely, those on the rotation curve dependency with time and radius, see Section 4.1.1).

One important consideration is that in the predicted gas surface density profiles (see Figures 14 and 15), our models reached lower values (approximately 0.1 dex) than those used by both Kennicutt (1998) (Figure 2) and our own fits for the star formation laws (Figure 6). A consequence of this is that we might be using too low star formation rate surface density values, giving that our star formation laws are too steep when low gas surface densities are considered. The data used in the fitting of the star formation laws are missing observations of the outermost regions of galaxies, despite still including some low-density regions. Therefore, it could be interesting to apply star formation laws which are not significantly extrapolating at low gas surface densities, for example by including (in the data used for fitting) lower gas density measurements. As such measurements are not yet available, this requires more observations to be made before attempting to determine a star formation law that does not extrapolate at low ($\Sigma_{gas} \lesssim 0.1 M_{\odot} pc^{-2}$) gas surface densities.

Another point of consideration regards the comparison of the models with the observed surface density profiles. When comparing to single galaxy measurements, the new star formation laws were in better agreement with the observations, however it should be noted that galaxies vary greatly in the behavior of their surface density profiles. While the models predictions were in strong agreement with observations (see Figures 19, 20a, and 20b) our comparison was based on a single galaxy (NGC2403). Therefore, it is clear that we cannot draw definitive conclusions about the predictive powers of the model on properties of galaxies such as gas, stellar, or baryonic surface density profiles. To obtain more significant conclusions, it would then be necessary to compare the model predictions with more galaxy surface density profiles.

4.1.1 Impact of Different Rotation Curve Assumptions

In addition to the star formation laws, further considerations can be made about the differences between this work and the other work which employed an inside-out growth mechanism but different assumptions for the rotation velocities (Costa, 2023). One of the main theoretical improvements of this work was the exponential radial dependence of the rotational velocity. This was a considerable improvement over previous works which instead considered a constant rotational velocity with radius. Employing exponential rotation curves allowed for more accurate prediction of the rotational velocities in the inner regions of galaxies, which often show lower values of v_{rot}. Additionally, this approach enables a proper estimate of the angular velocity ($\Omega = \frac{v_{rot}}{R}$), avoiding the issue of encountering infinities as $R \to 0$ kpc. As a consequence, this also allowed for the modeling of the Boissier law.
Another theoretical improvement was the inclusion of a rotational velocity which is constant in time, contrasting with the previous model where rotational velocity increased with time (following the assumption of the BTFR not evolving with time). This change was made to address an internal inconsistency in the previous model. In the previous approach, the rotational velocity increased with time, which resulted in an nonphysical increase of angular momentum. This modification of the model introduced a significant change in the results, as it caused lower gas fractions at the end of the evolution. This can be seen in Figure 23.

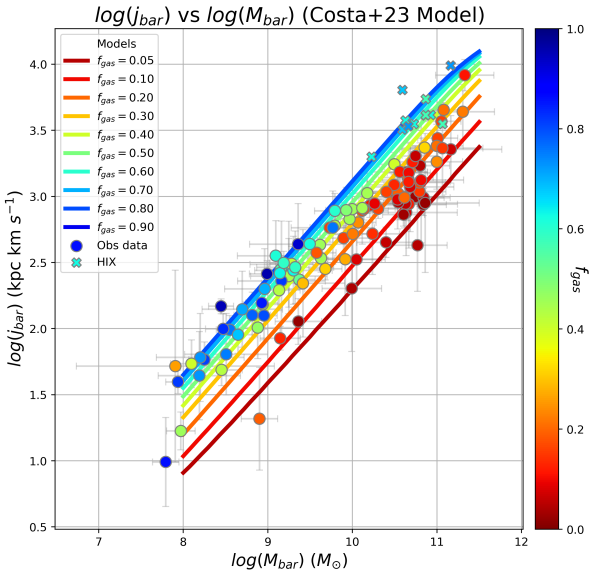

(a) Results from Costa (2023) Model with $v_{\rm rot}$ flat but evolving with time

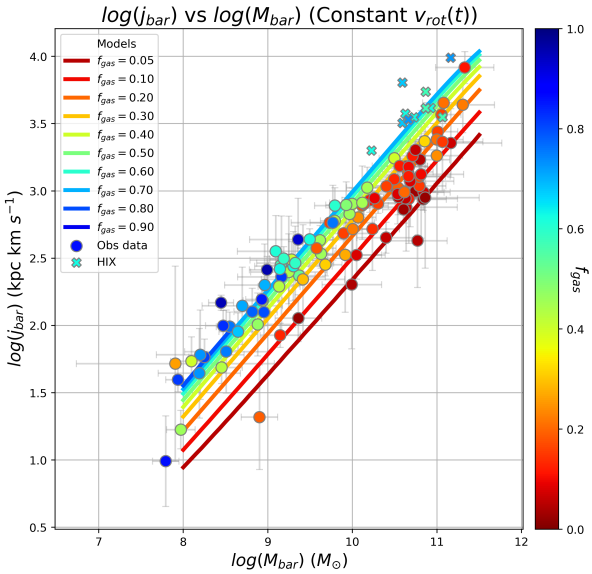

(b) Results from Costa (2023) Model with $v_{\rm rot}$ flat and independent on time

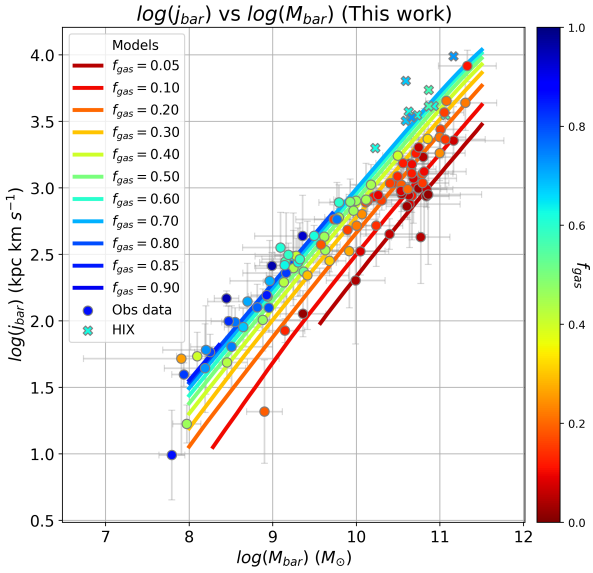

(c) This work

Figure 23: $j_{\rm bar} - {\rm M_{bar}} - f_{\rm gas}$ relation from different models: previous work (Costa, 2023) (a); results using the Costa (2023) model, only changing the assumption of the rotational velocity, which is now constant in time (b); results from this work (c). All the plots show the results assuming the standard KS law.

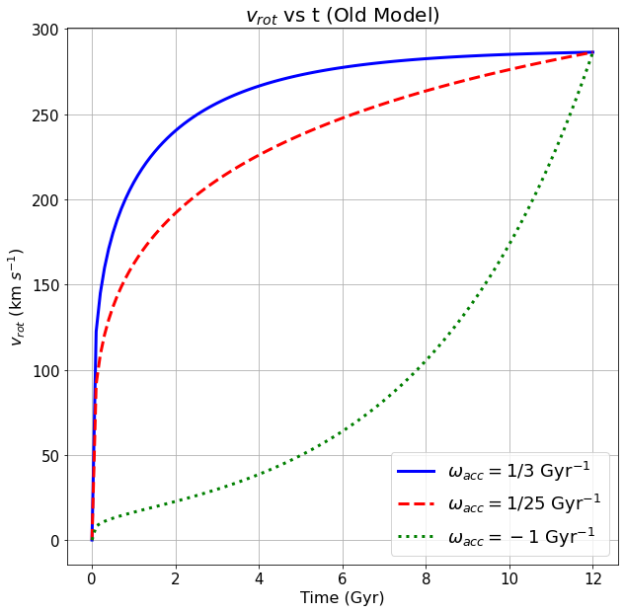

Figure 24: Temporal evolution of the rotation velocity, constant with radius, in the Costa (2023) model, for three accretion frequencies: $1/3$ (blue), $1/25$ (red), and -1 Gyr^{-1} (green).

Comparing the results seen in Figure 23a with Figure 23b, the predicted gas fractions at higher masses are lower by roughly 0.10. This could be explained by examining the behavior of the rotational velocity in the previous model (Figure 24). In contrast to a rotational velocity which is constant in time, and therefore does not depend on $\omega_{\rm acc}$, in the Costa (2023) model a highly negative accretion frequency (green dotted line) gives considerably lower rotational velocities even in the later stages of the evolution. By construction, at equal $j_{\rm acc}$ values, a lower $v_{\rm rot}$ corresponds to a higher $r_{\rm acc}$ and therefore more gas present at larger radii, where the star formation efficiency is lower. This causes larger $f_{\rm gas}$ with respect to a model in which the rotation curve is constant in time, as seen in Figure 23, and introduces already a significant change in the model predictions.

4.2 Limitations of the Model and Future Work

In this section, we will discuss the limitations and potential improvements to our model and methodology.

4.2.1 Accreting Angular Momentum

One of the main assumptions made in this model was an accreting specific angular momentum that increased with time with a constant slope of 1. This was done by introducing two parameters, k and n, which were both set to 1 (see Section 2.6). As outlined previously, the obtained range of baryonic specific angular momentum was not as large as in the previous Costa (2023) model, leaving more data points unpredicted (see Figures 23a and 23c). Hence, a straight-forward next step would then be to investigate how changing these parameters would impact the predictions of the models. In the context of the $j_{\rm bar} - {\rm M}_{\rm bar} - f_{\rm gas}$ relation, it could be interesting, for instance, to determine if different parameter values, using other star formation laws in addition

to the standard KS law, give results that are more in line with observations, and possibly if a more extended range of $j_{\rm bar}$ values could be obtained.

4.2.2 Rotation Curves

Another assumption that was made in this project was the radial dependence of the rotation curves. These were assumed to follow an exponential profile, which was a considerable improvement over previous works that instead assumed a flat rotation curve (i.e. constant with radius). However, this assumption is still not perfect, because it does not take into account peaks in the rotation curves that are often seen in higher mass galaxies, which are caused by galaxy bulges (see de Blok et al. (2008) and Lelli et al. (2016)). Assuming rotation curves that include this feature would further boost the accuracy of the model.

In the context of R_v, the data used in the fitting of the relation between R_v and $v_{\rm flat}$ showed a significant scatter and was not strongly correlated. While we proceeded with fitting for the purposes of this project, it remains to be determined if such a relationship exists. This could be achieved, for example, by considering datasets which have higher resolution and more measurements for each galaxy, such that the parameters are fitted more accurately. Alternatively, one may explore other parameterizations of the rotation curves.

4.2.3 Volumetric Star Formation Laws

In this project, we considered various versions of star formation laws, including the well-known Kennicutt-Schmidt law, the Boissier law, and a steeper variant of the KS law. This was done to simplify the model, as surface densities are easier to deal with both in theoretical modelling scenarios, as well as in observations. However, as previously mentioned, a star formation law based on surface densities faces the challenge of addressing the change in slope that occurs between low and high-density regimes (as seen in Figure 3). While including a dynamical timescale factor, like in the Boissier law, decreases this effect, another possibility is to consider volumetric star formation laws, instead.

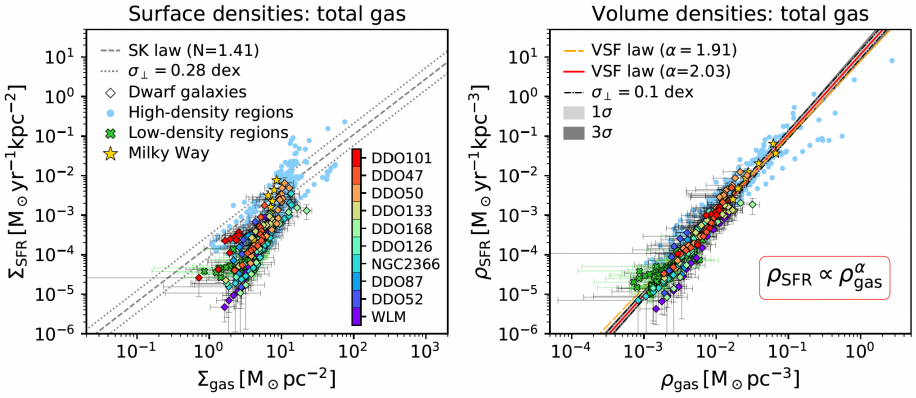

Figure 25: Comparison of star formation laws based on surface densities (left panel) versus volume densities (right panel). The plots show that the volumetric star formation densities are more tightly correlated with gas volume densities. Plots taken from Bacchini et al. (2020).

Bacchini et al. (2020) have shown that volumetric star-formation (VSF) densities have a tighter correlation with gas volume densities. A plot illustrating the difference between star formation laws with surface and volume densities can be seen in Figure 25. By employing a volumetric star formation law in future works, an investigation on how this impacts the gas fractions and specific angular momentum, and in turn the full $j_{\rm bar} - {\rm M}_{\rm bar} - f_{\rm gas}$ relationship, could be made. Despite the clear advantages, employing such a framework would require assumptions and constraints on the galaxy's gravitational potential, hydrostatic equilibrium, scale height, dark matter content, and velocity dispersion of the gas, which were all beyond the scope of this project.

5 Summary and Conclusions

This thesis investigated the baryonic specific angular momentum ($j_{\rm bar}$), mass ($\rm M_{bar}$), and gas fraction ($f_{\rm gas}$) relationship in galaxies, focusing on how different star formation laws influence this relationship. The study aimed to enhance previous disk evolution models by investigating different star formation laws in addition of the well-known Kennicutt-Schmidt law, as well as improve assumptions on the temporal and spatial rotational velocity dependencies.

In the disk evolution model we developed, the gas and stellar surface density profiles were calculated by solving the differential equations of disk evolution. We assumed an exponential gas accretion profile, which is described by the accretion frequency parameter, and that gas accretes inside-out.
We explored two additional star formation laws alongside the standard Kennicutt-Schmidt law: a revised version of the Kennicutt-Schmidt law and a law incorporating the angular speed of disk rotation. These laws were fitted using data that included low-gas density regions. Additionally, we fitted the rotation curves of a sample of galaxies from the SPARC catalogue using an exponential functional form, establishing a relationship between the fitted parameters.
For each star formation law, the model was evaluated in a range of values of present-day baryonic masses, and for each mass the gas accretion rate was varied using the accretion frequency parameter.

The results were able to quantitatively reproduce the $j_{\rm bar} - \rm M_{bar} - f_{gas}$ relation, returning reasonable gas fractions and baryonic specific angular momenta. The predicted surface density profiles were also in excellent agreement when compared with the example galaxy NGC 2403, however more work is needed on other galaxies in the sample to draw a firm conclusion. Interestingly, our results suggested that changing the star formation law does not have a large impact in the theoretical predictions of the model concerning the $j_{\rm bar} - \rm M_{bar} - f_{gas}$ relation. Instead, the dominant model ingredient was found to be the inside-out growth assumption. This implies that inside-out growth is a crucial ingredient in modeling the $j_{\rm bar} - \rm M_{bar} - f_{gas}$ relation, whereas star formation laws are relatively less significant. When comparing the predictions of the $f_{\rm gas} - j_{\rm bar}$ relation at fixed $\rm M_{bar}$ with observations, using the different star formation laws we saw that the standard KS law was able to return a larger range of $f_{\rm gas}$ values (in particular, it returned lower values of $f_{\rm gas}$ for lower $j_{\rm bar}$), compared to the two new laws we considered. We argue that this is due to the larger steepness of the star formation laws we introduced, however it cannot be definitely concluded which law works best in this regime due to the few observational data. Therefore, determining the shape of star formation laws in very low-density regions would seem an obvious improvement for future work when such measurement will become available.

Comparing our results to previous models such as the one presented by Costa (2023), we found that maximum $j_{\rm bar}$ values predicted were slightly lower in all mass regimes. This leaves more observational data unexplained by our models, and should therefore be improved in future attempts at reproducing the $j_{\rm bar} - \rm M_{bar} - f_{gas}$ relation. This could be achieved by exploring different values for the parameters that regulate the gas accretion in our formulation. Other points of future work concern an improved functional form of the spatial dependence of the rotational velocity, and the assumption of a volumetric star formation law, rather than one based on surface densities.

Acknowledgements

"Well, here at last, dear friends, on the shores of the Sea comes the end of our fellowship in Middle-earth. Go in peace! I will not say: do not weep; for not all tears are an evil."

– Gandalf the White, *The Return of the King*

While this thesis project has only spanned three months, it has been a deeply meaningful journey that I will cherish for years to come. I am fortunate to have spent nearly two years working on this intricate topic, which has not only provided me with substantial knowledge in the field but, most importantly, the opportunity to work with two incredible supervisors.

Filippo and Gabriele, throughout these two years, there have been numerous moments when I felt lost and uncertain, but you were always there to guide me. Filippo, you have been the most amazing supervisor anyone could ask for. From patiently explaining complex concepts multiple times to offering advice on personal matters, you were always present and approachable, helping me make the best decisions possible. I cannot express how truly grateful I am for your support. Gabriele, you have been an invaluable mentor for almost two years. Your help, whether it was with the smallest detail in my code, thesis, or with personal matters, has been immeasurable. I deeply respect both of you.

Special thanks to Pavel Mancera-Piña and Cecilia Bacchini for providing me with the observational data used in this project.

I would like to extend my gratitude to my colleagues at the Kapteyn Institute, Benjamin, George-Luca, Ines, Ioannis, Ivan, Jordy, Karol, Matei, for all the stimulating conversations. I would also like to thank my friends. Mo, whether I needed advice on a particular topic, someone to vent to about the stresses of exams, or just a buddy to unwind and play video games with, you were always there. Erik, Axel, and Kai, your support, camaraderie, and friendship have been invaluable throughout this journey, providing a much-needed break from the rigors of academic life with our gaming sessions. Akhil, going through university together with you made a huge difference, and your support through all the courses was priceless. Thank you all for being there for me.

I also want to extend my heartfelt gratitude to my girlfriend, Emma. We have been together for three years, and from the very beginning, you have understood my weaknesses and supported me through them. Your daily encouragement has been a pillar of strength, not just during this thesis, but throughout my entire degree. Our evening calls lifted my spirits even on the toughest days. Thank you from the bottom of my heart for always being by my side.

Lastly, I would like to thank my family, especially my father. Thank you for always pushing me to strive higher and believing in me. In moments of doubt, your simple yet profound advice always brought me back to a place of confidence. Dad, I have always looked up to you, and I am incredibly grateful for your unwavering support and wisdom.

References

Aumer M., Binney J. J., 2009, MNRAS, 397, 1286

Bacchini C., 2020, PhD thesis, University of Groningen, doi:10.33612/diss.133157780

Bacchini C., Fraternali F., Iorio G., Pezzulli G., 2019, A&A, 622, A64

Bacchini C., Fraternali F., Pezzulli G., Marasco A., 2020, A&A, 644, A125

Bigiel F., Leroy A., Walter F., Brinks E., de Blok W. J. G., Madore B., Thornley M. D., 2008, AJ, 136, 2846

Bigiel F., Leroy A., Walter F., Blitz L., Brinks E., de Blok W. J. G., Madore B., 2010, AJ, 140, 1194

Boissier S., Prantzos N., Boselli A., Gavazzi G., 2003, MNRAS, 346, 1215

Brook C. B., et al., 2012, MNRAS, 426, 690

Camilleri E., 2022, Bachelor's thesis, University of Groningen, https://fse.studenttheses.ub.rug.nl/id/eprint/28062

Chabrier G., 2003, PASP, 115, 763

Cimatti A., Fraternali F., Nipoti C., 2019, Introduction to Galaxy Formation and Evolution. From Primordial Gas to Present-Day Galaxies. Cambridge University Press (arXiv:1912.06216), doi:10.48550/arXiv.1912.06216

Costa A., 2023, Honors college project, University of Groningen

Di Teodoro E. M., Fraternali F., 2014, A&A, 567, A68

Di Teodoro E. M., Fraternali F., 2015, MNRAS, 451, 3021

Elmegreen B. G., 1997, in Franco J., Terlevich R., Serrano A., eds, Revista Mexicana de Astronomia y Astrofisica Conference Series Vol. 6, Revista Mexicana de Astronomia y Astrofisica Conference Series. p. 165

Elmegreen B. G., 2018, ApJ, 854, 16

Fall S. M., 1983, in Athanassoula E., ed., IAU Symposium Vol. 100, Internal Kinematics and Dynamics of Galaxies. pp 391–398

Frank B. S., de Blok W. J. G., Walter F., Leroy A., Carignan C., 2016, AJ, 151, 94

Frankel N., Sanders J., Rix H.-W., Ting Y.-S., Ness M., 2019, ApJ, 884, 99

Fraternali F., Tomassetti M., 2012, MNRAS, 426, 2166

Gatto A., Fraternali F., Read J. I., Marinacci F., Lux H., Walch S., 2013, MNRAS, 433, 2749

González Delgado R. M., et al., 2015, A&A, 581, A103

Hoyle F., 1949. p. 195

Hunter D. A., et al., 2012, AJ, 144, 134

Iorio G., Fraternali F., Nipoti C., Di Teodoro E., Read J. I., Battaglia G., 2017, MNRAS, 466, 4159

Kennicutt R., 1998, ApJ, 498, 541

Kennicutt Robert C. J., et al., 2007, ApJ, 671, 333

Kroupa P., Tout C. A., Gilmore G., 1993, MNRAS, 262, 545

Kurapati S., Chengalur J. N., Pustilnik S., Kamphuis P., 2018, MNRAS, 479, 228

Larson R. B., 1976, MNRAS, 176, 31

Lelli F., McGaugh S. S., Schombert J. M., 2016, AJ, 152, 157

Lelli F., McGaugh S. S., Schombert J. M., Desmond H., Katz H., 2019, MNRAS, 484, 3267

Leroy A. K., Walter F., Brinks E., Bigiel F., de Blok W. J. G., Madore B., Thornley M. D., 2008, AJ, 136, 2782

Mancera Piña P. E., Posti L., Fraternali F., Adams E. A. K., Oosterloo T., 2021a, A&A, 647, A76

Mancera Piña P. E., Posti L., Pezzulli G., Fraternali F., Fall S. M., Oosterloo T., Adams E. A. K., 2021b, A&A, 651, L15

Marasco A., Cresci G., Posti L., Fraternali F., Mannucci F., Marconi A., Belfiore F., Fall S. M., 2021, MNRAS, 507, 4274

McGaugh S. S., 2012, AJ, 143, 40

McQuinn K. B. W., Skillman E. D., Dolphin A. E., Mitchell N. P., 2015, ApJ, 808, 109

Mo H., van den Bosch F. C., White S., 2010, Galaxy Formation and Evolution

Murray N., Rahman M., 2010, ApJ, 709, 424

Obreschkow D., Glazebrook K., 2014, ApJ, 784, 26

Patel S. G., et al., 2013, ApJ, 766, 15

Peebles P. J. E., 1969, ApJ, 155, 393

Pezzulli G., Fraternali F., 2016, MNRAS, 455, 2308

Pezzulli G., Fraternali F., Boissier S., Muñoz-Mateos J. C., 2015, MNRAS, 451, 2324

Pilkington K., et al., 2012, A&A, 540, A56

Prantzos N., 2008, in Charbonnel C., Zahn J. P., eds, EAS Publications Series Vol. 32, EAS Publications Series. pp 311–356 (arXiv:0709.0833), doi:10.1051/eas:0832009

Putman M. E., Peek J. E. G., Joung M. R., 2012, ARA&A, 50, 491

Romanowsky A. J., Fall S. M., 2012, ApJS, 203, 17

Sancisi R., Fraternali F., Oosterloo T., van der Hulst T., 2008, A&ARv, 15, 189

Sandstrom K. M., et al., 2013, ApJ, 777, 5

Schmidt M., 1959, ApJ, 129, 243

Silk J., 1997, ApJ, 481, 703

Sparke L., Gallagher J., 2007, Galaxies in the Universe: An Introduction. Cambridge University Press

Stevens A. R. H., Lagos C. d. P., Obreschkow D., Sinha M., 2018, MNRAS, 481, 5543

Tully R. B., Fisher J. R., 1977, A&A, 54, 661

Zhang H.-X., Hunter D. A., Elmegreen B. G., Gao Y., Schruba A., 2012, AJ, 143, 47

Zoldan A., De Lucia G., Xie L., Fontanot F., Hirschmann M., 2018, MNRAS, 481, 1376

de Blok W. J. G., Walter F., Brinks E., Trachternach C., Oh S. H., Kennicutt R. C. J., 2008, AJ, 136, 2648

Appendix A

In Figure A we show the marginalized posterior probabilities of the free parameters of the star formation laws fits.

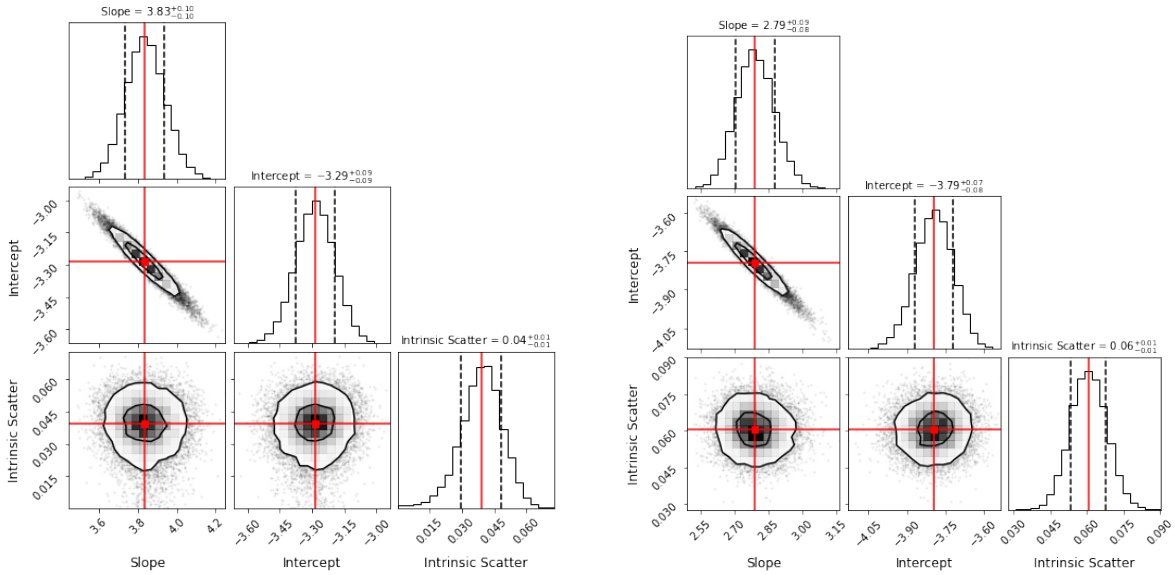

(a) Kennicutt-Schmidt

(b) Boissier

Figure A: Marginalized posterior probabilities of the free parameters from the Bayesian fitting algorithm (Lelli et al., 2019). The left corner plot shows the maximum likelihood parameters for the Kennicutt-Schmidt law fitting, whereas the right plot shows the maximum likelihood parameters for the Boissier law fitting.

All the parameters are well constrained and clearly indicate that there exists a relationship between the star formation rate and gas surface densities.